6-10-2022

Electron Backscatter Diffraction Analysis of Olivine in Ureilite Meteorites: Evaluation of the Partially Magmatic Catastrophic Disruption Model of the Ureilite Parent Body (UPB)

James Karl Frye
Portland State University

Electron Backscatter Diffraction Analysis of Olivine in Ureilite Meteorites: Evaluation of the Partially Magmatic Catastrophic Disruption Model of the Ureilite Parent Body (UPB)

by

James Karl Frye

A thesis submitted in partial fulfillment of the
requirements for the degree of

Master of Science
in
Geology

Thesis Committee:
Alexander Ruzicka, Chair
Richard Hugo
Melinda Hutson

Portland State University
2022

Abstract

Past studies of olivine have yielded insights into crystallographic slip systems and how they are activated thermally. Using this information in conjunction with Electron Backscatter Diffraction (EBSD) analysis and metrics developed for chondrites, I constrained the thermal environment and the cooling rate for four ureilite meteorites in an attempt to test the model of catastrophic disruption of the ureilite parent body while it was partly molten. Present evidence for deformation, along with thermal metrics, were examined in order to conclude the following: Deformation of the meteorites took place at high temperatures followed by swift cooling, leaving little time for annealing. Most samples yielded deformation estimates of 800 ^{o}C-1000 ^{o}C, lower than the anticipated range of 1200 ^{o}C-1300 ^{o}C. Annealing results were low, indicative of quick cooling rates, as expected based on prior studies. Overall the data support the catastrophic hot disruption model.

Acknowledgments

First, I would like to thank Dr. Alexander Ruzicka, who made the culmination of this project possible with his unwavering support and patient guidance. I would also like to extend my gratitude to the rest of my committee; Dr. Richard Hugo and Dr. Melinda Hutson who offered indispensable feedback and suggestions that helped make this work the best it could be.

Furthermore, I would like to extend my most heartfelt gratitude to Kimberly Maccini for her mentorship and assurance throughout this process and for helping me to stay positive and believe in myself. Moving across the country during a global pandemic and encountering rampant wildfires during my first week of residency was an unparalleled life challenge yet your advice and lively encouragement, kept my spirits up during tumultuous times.

I also am so grateful to so many other individuals in the Portland State University Geology Department who helped in so many different ways to make this journey possible.

Table of Contents

List of Tables

List of Figures

1) INTRODUCTION

The field of meteoritics is a burgeoning subfield of geology. Meteorites offer opportunities to investigate the composition and formation processes of extraterrestrial bodies and offer insights into the evolution of the solar system. For this study ureilites are the meteorites of interest.

Ureilites compose the second largest group of achondrite (igneous) meteorites. They are olivine-rich (ultramafic), with low- Ca pyroxene in the form of pigeonite. The majority of ureilites are unbrecciated, monomict rocks with coarse olivine and pyroxene grains which range from euhedral to subhedral (Goodrich et al., 2004). Carbon phases in ureilites can be found in the form of graphite and high-pressure polymorphs such as diamond or lonsdaleite, and are thought to have formed by intense shock from impacts (Herrin et al., 2010; Nestola et al., 2020). Troilite and Fe- Ni metal phases are also present in these meteorites, in the form of rounded blebs.

Ureilites are generally thought to be derived from the mantle of a single differentiated, partly molten planetesimal (the ureilite parent body, or UPB) which was heated internally (Rai et al., 2020). The parent body is estimated to have been ~ 250 km in diameter (Wilson et al 2008: Michel et al., 2014). The UPB was catastrophically disrupted by a major impact ~5 Ma after the formation of calcium aluminum inclusions (CAI), which is the earliest dated solar system material (Wilson et al, 2008). Presumed catastrophic disruption and the onset of rapid cooling is thought to have occurred while the parent body was partly molten (Herrin et al., 2010; Michel et al., 2014; Rai et al., 2020; Nestola et al., 2020). Temperatures are constrained to have been 1,200 ^{o}C-1,300

^{o}C using pyroxene geothermometry of grain cores (Herrin et al., 2010) and graphite ordering (Barbaro et al., 2020). Rapid cooling is inferred based on preservation of chemically uniform grain cores and narrow zoned rims for olivine and pyroxene, which appear to indicate cooling 0.05–10 ^{o}C hr $^{-1}$ (Herrin et al., 2010: Goodrich et al., 2004). Past studies of ureilite formation support a catastrophic collision with the partly molten Ureilite Parent Body (UPB) leading to fragmentation, quenching, and re-accretion (Herrin et al., 2010; Michel et al., 2014; Rai et al., 2020; Nestola et al., 2020). Geothermometry, elevated Ca contents in olivine, a graphite-diamond mix, and uniform olivine and pyroxene core compositions with reduction rims, all suggest rapid cooling from magmatic temperatures (~1250 ^{o}C) post collision (Barbaro et al. 2020). There is still significant uncertainty surrounding the size and degree of chemical differentiation of the UPB.

This project involves utilizing Electron Backscatter Diffraction (EBSD) temperature and annealing metrics developed for olivine by Ruzicka and Hugo (2018), in order to constrain the deformation and thermal histories of four ureilite meteorites. In order for the popular model to be supported, results must yield high thermal values and low annealing values, which would be consistent with catastrophic disruption while hot and swift post shock cooling of fragments.

1.1 Ureilite Parent Body:

Fig. 1 presents a schematic which consists of 6 major events. Step [1] represents the initial accretion of the UPB approximately 1-2 Ma after CAI (Barbaro et al., 2020). Due to the time frame of accretion ^{26}Al was an abundant radioactive isotope in the nebular accretionary disk with a half-life of 7.17×10^5 years. Decay of this isotope is what enabled internal heating and chemical differentiation of the body, seen in step [2]. Event [3] represents the catastrophic disruption of the UPB at 5 Ma after CAI. Step [4] depicts the re-accretion of fragments into daughter bodies. This process is responsible for polymict brecciated ureilites (e.g., Goodrich et al., 2004; Downes et al., 2008; Barbaro et., al 2020). Re-accretion would have happened for all ureilites (Herrin et al., 2010). Steps [6] and [7] represent transport, entrance into the Earth atmosphere, and sample recovery.

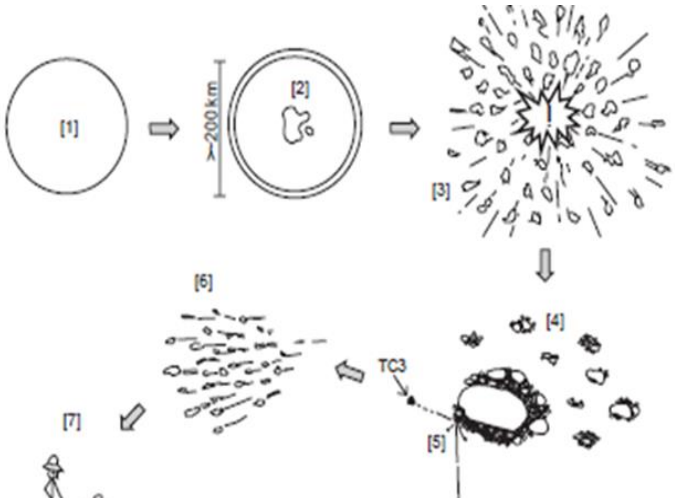

Figure 1. Image acquired from Herrin et al. (2010). Depicts the constrained evolution of ureilite formation: [1] Accretion. [2] Heating and melting from ^{26}Al decay, igneous processes, differentiation. [3] Catastrophic impact/disruption and fragmentation. [4] Cooling and cold history [5] Re-accretion into daughter bodies or source bodies. [6] Transport. [7] Terrestrial weathering and discovery.

1.2 Petrogenesis and heterogeneity:

Though the ureilite parent body could have been disrupted while hot, it may have been only partly molten at this time. The degree of partial melting for ureilites from a chondrite like protolith is typically estimated at approximately 20–30% (Herrin et al.,

2010). Evidence suggests the protolith never experienced a homogeneous melt residue, which is supported by Mg# variations and diverse oxygen isotope ratios of recovered ureilites (Goodrich et al., 2000; Downes et al., 2008). Ureilites are regarded as residues, or the unmelted parts of a magmatic system (Goodrich et al., 2004), as opposed to cumulates (Berkeley et al., 1980), which would have crystallized from melts and which would imply a larger degree of melting. The implication for a higher degree of melting if the olivine were cumulates is due to olivine's comparatively high melting temperature. In order for olivine to form as a result of crystal fractionation a majority of the UPB would have needed to undergo melting.

One of the ways chemical variations are measured is with Mg#'s ((Mg/(Mg+Fe))*100) which is the ratio of magnesium to iron in an igneous rock. The presence of several different distinct lithologies in polymict ureilities provides evidence that there was compositional heterogeneity within the UPB. FeO-reduction rims are a common feature of olivine in ureilites and support the assertion that ureilites are derived from a singular planetesimal, despite the noted chemical heterogeneity in Mg#. Varying oxygen isotope ratios also provide evidence of a single body with residue heterogeneity. Oxygen isotopes range along a $d^{17}O–d^{18}O$ line of slope ~1 coincident with the Carbonaceous Chondrite Anhydrous Mineral (CCAM) line, opposed to the terrestrial fractionation line of which differentiated bodies such as Earth and Mars are found on (Goodrich et al., 2004).

1.3 Disruption and re-accretion:

Disruption of the UPB took place ~5 Ma after CAI (Wilson et al., 2008). Past studies of ureilites have constrained the temperature to be 1200 ^{o}C -1300 ^{o}C at the time of disruption (Barbaro et al., 2020). For ureilites, disrupted semi-molten fragments would have been exposed to low ambient temperatures in space, leading to rapid cooling or quenching of the hot fragments. The rate of cooling in ureilites is characterized as 0.05–10 ^{o}C hr^{-1} (Herrin et al., 2010: Goodrich et al 2004), which is indicative of a quick rate of cooling.

Ureilites consistently show significant evidence for shock deformation, in the form of both high-pressure polytypes of carbon (diamond and lonsdaleite), and the appearance of shock deformed olivine, which shows non-uniform extinction when viewed in cross-polarized transmitted light (Herrin et al., 2010). Shock deformation can be characterized both by using the Stöffler et al. (1991) shock classification system (Table 1), as well as by the weighted shock stage scheme of Jamsja and Ruzicka (2010), which provides a more detailed characterization of shock effects in olivine.

Re-accretion into daughter bodies is thought to have occurred. Cosmic Ray Exposure (CRE) ages that have been acquired for ureilites do not fit the time frame of catastrophic disruption (Leya and Stephenson 2019). This means that ureilites must have been stored in daughter bodies, until the time that the collision that sent these meteorites Earth bound occurred. Further, studies of the Almahata Sitta (AHS) ureilite and other polymict breccias serve as strong evidence that re-accretion of various lithologies occurred.

1.4 The Role of Olivine:

Table 1: Stöffler et al. (1991) shock stages and features in olivine and plagioclase.

Shock Stage	Effects resulting from equilibration peak shock pressure		Effects resulting from local P-T-excursions	Shock pressure Gpa*	Post-shock temperature increase °C**	Estimated minimum temperature increase °C
	olivine	plagioclase				
Unshocked S1	Sharp optical extinction. Irregular fractures		None	<4-5	10-20	10
Very Weakly Shocked S2	Undulatory extinction. Irregular fractures		None	5-10	20-50	20
Weakly Shocked S3	Planar fractures undulatory extinction irregular fractures	Undulatory extinction	Opaque shock veins incipient formation of melt pockets, sometimes interconnected	15-20	100-150	100
Moderately Shocked S4	Mosaicism (weak), planar fractures	Undulatory extinction, parially isotropic, planar deformation features	Melt pockets, interconnecting melt veins, opaque shock veins	30-35	250-350	300
Strongly Shocked S5	Mosaicism (strong), planar fractures + planar deformation features	Maskelynite	Pervasive formation of melt pockets, veins and dikes: opaque shock veins	45-55	600-850	600
Very Strongly Shocked S6	Restricted to local region in or near melt zones		As in stage 5			
	Solid state recrystallization and staining, ringwoodite, melting	Shock melted (normal glass)		75-90	1500-1750	1500
Shock Melted	Whole rock melting (impact melt rocks and melt breccias)					

The focus of this study is on olivine (Mg_2SiO_4) which predominantly comprises these ureilites. It is a mineral that is also found in chondrites. As such, it is an excellent mineral to study in meteorites due to its abundance in chondritic and achondritic solar system material. Furthermore, deformation experienced by meteorites can be recorded in the crystalline lattice of olivine crystals and coincides with specific levels of shock S1-S6 (Non-shocked – highly shocked and recrystallized). How olivine deforms can be related to features of the environment. An olivine grain is portrayed in Fig. 2 along with some of its features, (hkl) represents a crystal plane, [hkl] corresponds to crystal direction, <hkl> represents a family of crystal directions, and {hkl} represents a family of crystal planes. The [100], [010], and [001] correspond to different crystal axes directions which are referred to in Fig. 2, as a, b, and c respectively. Misorientation can happen along an axis as a result of dislocations.

Dislocations are crystal defects along which a discontinuity occurs in the crystal lattice. The two we are concerned with are edge dislocations which correspond to tilt boundaries, and screw dislocations which are associated with twist boundaries. These slip systems and boundaries are depicted in Fig. 3. Of the component parts of edge dislocation slip systems there is the slip plane, the slip direction, and the crystal rotation axis. The slip plane is the plane in which the deformation occurs and is well defined as a single plane for edge dislocations. For screw dislocations, there is not necessarily a single plane along which motion occurs. The slip direction is the vector of motion in the crystal. As such, the slip direction will be along the slip plane. The crystal rotation axis is the imaginary axis in which rotation of the crystal or misorientation is taking place. This

crystal rotation axis in an olivine crystal frame can be portrayed in a crystal rotation axis (CRA) plot as shown on figure 3a, and can be composed of a tilt (Fig. 3b) or twist boundary as highlighted in figure 3c. How the crystal deforms relies on the factors of the environment such as temperature, pressure, and water content (Karato et al., 2007). For both edge and screw dislocations, the rotation axes for crystal misorientations are perpendicular to the slip directions.

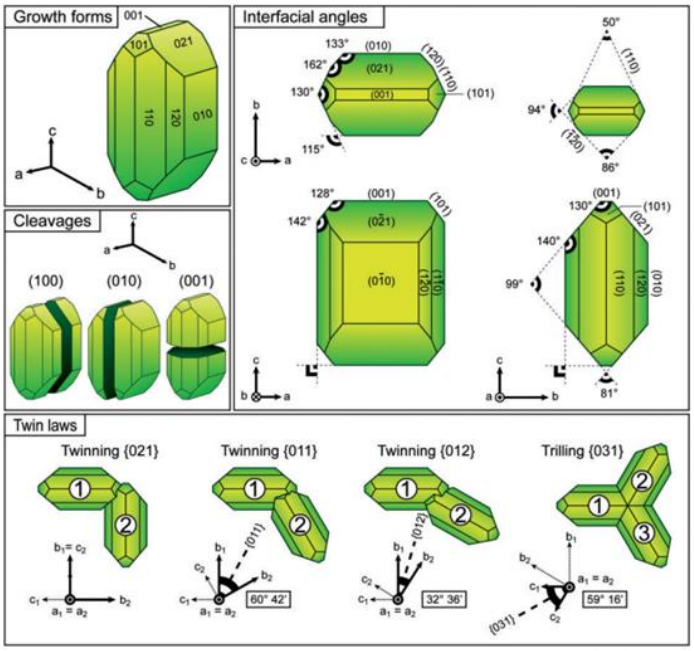

Figure 2. Acquired from Welsch et al (2013). Image depicts the structural properties of an olivine crystal grain. Includes growth form, Cleavage, interfacial angles, and twin laws. Growth forms depicts planes geometric planes of the mineral. Cleavages presents the cleavage planes of the olivine crystal.

These slip systems result in localized misorientations of the crystalline lattice that can be observed optically via the extinction of olivine under crossed polarized light microscope. Not only are these misorientations identifiable with optical microscopes they can also be mapped utilizing Electron Backscatter Diffraction (EBSD).

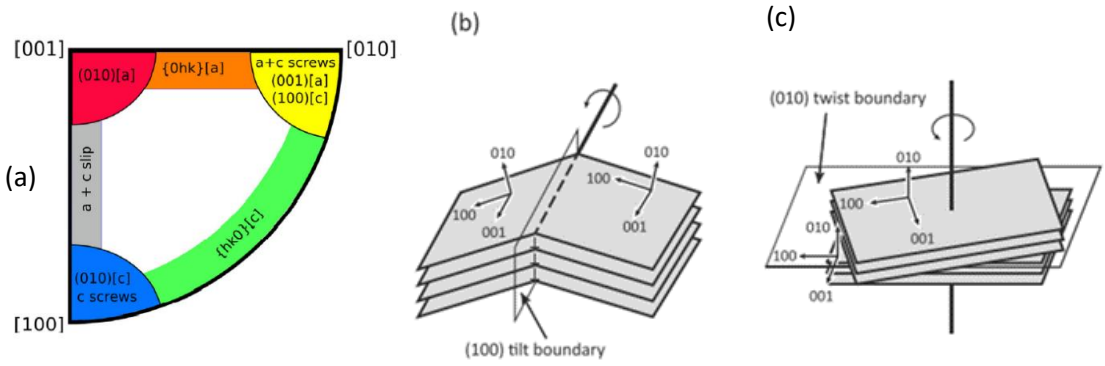

Figure 3. Image (a) acquired from Ruzicka and Hugo 2018 depicts a CRA diagram with Crystal Rotation Axes expressed in [hkl] outside the correspondent field (blue-red). Slip direction is expressed as [a], [band/or [c] within the correspondent fields. Slip planes are expressed as (hkl) or {hkl}. Image (b-c) acquired from Chatzaras et al., (2016) portrays the relationship of rotation axis to tilt (b) and twist misorientation boundaries (c). (b): rotation axis in [001] direction on a (100) tilt boundary, example (c): rotation axis in [010] direction on a (010) twist boundary).

The slip direction is parallel to the dislocation Burgers (**b**) vector, which represents the magnitude and direction of the lattice distortion. When determining slip direction, the shortest atomic displacement is favored because of the lower strain energy associated with dislocation formation and motion. In olivine this is either **b** = [100] (0.476 nm at ambient condition) or **b** = [001] (0.598 nm) (Karato et al 2007). However, the difference in the length of these two Burgers vectors is minute, and a change in the physical or chemical environment could alter the dominant slip direction. This change can be associated with the change in pressure, temperature, and or water content. The choice of the slip plane is determined by more factors. The magnitude of the Peierls stress (resistance to shear at T = 0 K) is what determines the choice of a slip plane (Karato et al., 2007). For a given Burgers vector, the favored slip plane is the one for which h/**b** (h is the distance between slip planes, **b** is the length of the Burgers vector) is the largest (Karato et al., 2007).

Studies show that (a) at high temperature and low strain rate, the dominant slip system in olivine is [100] (010); (b) at modest temperature and strain rate, the dominant slip direction remains [100], but slip occurs using many different slip planes; and (c) at low temperature and high strain rate, the dominant slip direction changes to **b** = [001] (the slip plane is either (010) or (100) or both (Karato et al., 2007)). Water enhances variable slip systems in response to stress but especially [001] slip (Karato et al., 2007), whereas pressure enhances [100] slip (Carter et al., 1968; Carter and Ave'Lallemant 1970). Olivine has a preferred slip direction of [100] when hot, and [001] when cold (Carter et al., 1968; Carter and Ave'Lallemant 1970). Extrapolating the strain rate and pressure dependencies, found by the latter authors, to shock conditions suggests that temperature will be the primary control on slip directions (Ruzicka and Hugo, 2018).

2) METHODS AND SAMPLES

A Leica DM2500 petrographic microscope was used to study nine thin sections of different ureilites to characterize the shock stages using the Stöffler et al. (1991) classification features for olivine, as seen in Fig. 4. Weighted shock stages are also provided in accordance with Jamsja and Ruzicka (2010) in Fig. 4. Petrographic Thin Sections (PTS) were observed in Crossed Polarized Light (XPL), Plane Polarized Light (PPL), and Reflected Light (RL). Primary shock stage analysis was conducted in PPL and XPL in which extinction angle and planar fracture sets of olivine were analyzed and recorded for each grain. In RL, FeO-reduction rims were observed and characterized along with the abundance of metal and troilite. From the initial nine samples, four were selected for EBSD analysis. Preference was given to less weathered specimens with variable shock stages S3-S6. The four selected ureilites were: Northwest Africa (NWA) 11993, NWA 12433, NWA 7630, and NWA 7304. Data for these samples, derived from the Meteoritical Bulletin Database (MBD, 2022), along with the specific thin sections studied, is given in Table 2.

Thin sections were polished with a .065 µm colloidal silica solution in 20-minute increments for a cumulative time of ~ 60-65 minutes. Samples were then given a ~5 nm carbon coat in preparation for EBSD analysis.

Table 2: Meteoritic Bulletin information for four ureilites

Meteorite	PTS CML #	Petrography	Mineral comp	S.S
NWA 11993	CML 0681-2	Predominantly olivine and pigeonite grains ~ 1mm in diameter. Separated by fine grained materials, cracks or Fe-hydroxide weathering product. No metal or sulfides were found.	Ferroan olivine cores (Fa22.6±0.7, N = 38) and rims are more magnesian (Fa15.6±3.6, N = 9). Pigeonite (Fs17.1±3.8Wo11.1±3.5, N = 28)	S4
NWA 12433	CML 0975-2A	Contains olivine and pigeonite grains up to 1-2 mm across. Some areas opaque in transmitted light occur interstitial to olivine and pyroxene and cross-cut these grains. Opaque areas are largely filled by weathering products or other fine-grained material and feature tabular to acicular grains of graphite up to 200 μm long.	Olivine grains have homogenous, ferroan cores (Fa22.5±0.2, N = 18) and more magnesian rims (Fa15.2±2.3, N = 18), low Ca-pyroxene is relatively homogeneous (Wo 9.5±0.0, Fs18.8±0.1, N = 15).	NP
NWA 7630	CML 1371-2	Protogranular aggregate of predominantly (>90 vol.%) olivine with reduced metal-bearing rims plus minor pigeonite.	Olivine (cores Fa21.1-21.3; rims Fa12.3; Cr2O3 = 0.7 wt.%), pigeonite (Fs17.2-17.8Wo6.1-6.0)	Low
NWA 7304	CML 0614-2	An olivine-rich rock (>75%) with low-Ca pyroxene, graphite laths to 1 mm, and Fe-oxide and hydroxide minerals (hematite, goethite, and common hematite-magnetite mixtures). Ca-sulfate is rarely present in veins. Olivine-rich and pyroxene-rich regions are ~1 mm in diameter. Olivine-rich areas are partly recrystallized (shock stage S6) and have recrystallized domains showing one dominant lineation, but are mainly composed of small (<10 μm diameter) subhedral olivine grains with interstices between olivine (<3 μm wide) filled	Fine-grained, olivine-rich areas far from graphite contain relatively ferrous olivine (Fa22.3±0.3, Fe/Mn = 49±11 at., n=28) and low-Ca pyroxene (Wo4.4±1.5 Fs21.2±1.0, n=10), whereas closer to graphite, olivine (Fa8.1±2.5, Fe/Mn = 17±4 at.%, n=11) and low-Ca pyroxene (Fs12.4±1.8Wo2.8±0.9, n=9) are more magnesian	High

		by low-Ca pyroxene, high-Ca pyroxene, and chromite. Interstitial regions between millimeter-sized olivine areas are rich in pyroxene, Fe-oxide and hydroxide phases, and graphite, the latter partly replaced by Fe-oxide minerals.		

*S.S stands for the conventional shock stage Stöffler et al. (1991)
*NWA is short for North West Africa followed by the meteorite number, this is common meteorite nomenclature for finds from northern Sahara
*CML: Cascadia Meteorite Laboratory
*PTS is Petrographic thin section
*NP: Not Present

The SEM-EBSD system that was used for this study is a Zeiss Sigma Variable Pressure-Field Emission Gun-Scanning Electron Microscope (VP-FEG-SEM), with an Oxford Instruments ULTIM MAX 65 energy dispersive spectrometer (EDS) with silicon-drift detector, and an Oxford Instruments Symmetry EBSD detector. These are available at the CEMN facility at PSU. For EBSD, the SEM was operated at 20 keV accelerating voltage. Samples were tilted in SEM at 70^{o}. EDS yielded chemical data for map areas. EDS images were collected in tandem with Electron Backscatter Diffraction (EBSD) patterns (also known as Kikuchi patterns). These patterns give information on the phase, orientation, and diffraction intensity (Band Contrast) of each pixel in a map. From this data other features and quantities are calculated.

EDS and EBSD data were processed with integrated Oxford Instruments software, AZtec 4.3 and AZtecCrystal 1.1, using methods similar to those of Ruzicka and Hugo (2018). EBSD analysis was conducted using AztecCrystal 1.1. No wild spike removal or post acquisition cleaning was carried out on the data suites. In AZtecCrystal two universal grain parameters were set which included (1) defining a “grain” as having a

minimum of 5 contiguous pixels and (2) defining critical misorientations of 15^{o} as grain boundaries. Primary minerals of interest are olivine, pyroxene, high calcium-pyroxene, and graphite which correspond to EBSD minerals forsterite, pigeonite, diopside, and graphite respectively. Deformation in olivine is the primary focus of this study. The deformation temperature and post-deformation annealing parameters for olivine were determined using the Ruzicka and Hugo (2018) methodology explained in more detail below. Large Area Maps (LAMs) were obtained for each thin section, and Targeted Maps (TMs) were obtained for all meteorites except NWA 7304. The LAMs provide the best data sets for determining the overall temperature and annealing parameters, whereas targeted maps show more detailed features for selected regions. Table 3 presents the number of fields, step size, pixel number and surface area analyzed for the four LAM and subsequent targeted maps of the four samples.

Images from these analyses were constructed and interpreted with their findings expressed in the results section herein. EBSD data was subsetted into coarse and fine grain size populations for each meteorite to see if there was a difference between the grain size fractions. Individual images were montaged together to depict features in the LAMs and TMs. This included Band Contrast (BC) images which are derived from Kikuchi band intensity, and Phase maps (Ph), which depict the identified phases of the grains. For olivine and pyroxene, the most important phases to this study, Inverse Pole Figure (IPF) maps portray the orientation of crystal grain axes relative to the sample directions (x, y, z). Deformation was depicted in the samples with the following three maps: (1) Kernel Average Misorientation (KAM) which is the average relative

orientation of 11 neighboring pixels to a central pixel. (2) Grain Reference Orientation Deviation- Angle (GROD-Ang) maps, which portray the mean misorientation of each pixel from the referential mean for the entire grain. (3) Grain Orientation Spread (GOS), expressed as Mean Orientation Spread in AztecCrystal software, depicts average misorientation in grains and is used as a measure of deformation intensity. Grain boundaries in this work are defined as being misorientations > 15º. Subgrain boundaries are defined in this work as being misorientations <15º. Special Boundaries (SB) are user defined map parameters, in which the grain boundaries rotation axes are within 5º of the <001>, <010>, <100>, or <101> directions. The Multiples of Uniform Density MUD values expressed in the Crystal Rotation Axis (CRA) diagrams were used to calculate R2-10º as well as R.5-2º. CRA diagrams were contoured to a 25º halfwidth to better depict broad trends, as described in Ruzicka and Hugo (2018).

Sk. and $R_{2\text{-}10}$, are the primary EBSD deformation metrics used in this study for olivine, these metrics are further defined as (1) GOS skewness (Sk = mean/median GOS), which is a measure of deformation heterogeneity and which can constrain post-deformation annealing (Ruzicka and Hugo 2018). Sk is the primary annealing parameter of this study. Annealing is defined as the migration of crystal deformation to edges or high misorientation focal points in the crystal as a result of dislocation climb, enabled by elevated temperatures for a prolonged period of time. High annealing is reflected in high skewness values. High skewness values can also be an indication of recrystallization which is the process of replacing extensively deformed grains with new grains that nucleate and grow, using up the “parent grain” in the process. This process can occur

swiftly and is not indicative of a slow cooling rate. (2) The primary thermal deformation parameter is expressed as $R_{2\text{-}10}$ which is related to the relative directions of 2-10° rotation misorientations in an olivine crystal frame, which in turn is related to deformation slip systems, and which can used to constrain deformation temperature (Ruzicka and Hugo 2018). R was calculated with the following equation:

F[001]+F[010]/F[001]+F[010]+F[100]. F represents the frequency of crystal rotation misorientations along subgrain boundaries. R values were also calculated for .5-2^{o} misorientation, however this data was more noisy and is useful only as a point of comparison to the more representative $R_{2\text{-}10}$ values. This section, and the preceding ones, at times become acronym and terminology heavy. In an attempt to help make this work easier to follow, the acronyms of this section are listed in Table 4 along with their respective meanings.

Table 3: Meta data for LAM and TMs

Meteorite	Maps	Step Size (μm)	Fields	# pixels	Area analyzed (μm^2)	Area analyzed (mm^2)
NWA 11993	LAM	5	292	8445888	2.11E+08	2.11E+02
	TM 1	2	1	187125	7.49E+05	7.49E-01
	TM 2	0.9	1	515016	4.17E+05	4.17E-01
	TM 3	1.4088	2	1004679	1.99E+06	1.99E+00
	TM 4	0.9	1	348672	2.82E+05	2.82E-01
	TM 5	0.9	1	394400	3.19E+05	3.19E-01
NWA 12433	LAM	4	119	5473563	8.76E+07	8.76E+01
	TM 1	1.7	1	216008	6.24E+05	6.24E-01
	TM 2	0.93	1	216008	1.87E+05	1.87E-01
	TM 3	2.5	1	99736	6.23E+05	6.23E-01
	TM 4	1.8	1	251865	8.16E+05	8.16E-01
	TM 5	1	1	224817	2.25E+05	2.25E-01
	TM 6	0.8921	1	224817	1.79E+05	1.79E-01
NWA 7630	LAM	4.5	186	6548715	1.33E+08	1.33E+02
	TM 1	1.4	1	256376	5.02E+05	5.02E-01

	TM 2	1	1	93280	9.33E+04	9.33E-02
	TM 3	2	1	287835	1.15E+06	1.15E+00
	TM 4	2	1	73320	2.93E+05	2.93E-01
	TM 5	3.2	1	181179	1.86E+06	1.86E+00
	TM 6	1.6	1	169575	4.34E+05	4.34E-01
	TM 7	1	1	150192	1.50E+05	1.50E-01
NWA 7304	LAM	1	36	8939520	8.94E+06	8.94E+00

Table 4: Acronyms

Acronyms	
PTS	Petrographic thin section
XPL	Crossed Polarized Light
PPL	Plane Polarized Light
RL	Reflected Light
EBSD	Electron Backscattered Diffraction
NWA	Northwest Africa
MBD	Meteoritical Bulletin Database
SEM	Scanning Electron Microscope
EDS	Energy Dispersive Spectroscopy
LAM	Large Area Map
TM	Target Map
BC	Band Contrast
Ph	Phase
IPF	Inverse Pole Figure
KAM	Kernel Average Misorientation
GROD ang	Grain Reference Orientation Deviation Angle
GOS	Grain Orientation Spread
GB	Grain Boundary
SB	Special Boundary
MUD	Multiples of Uniform Density
CRA	Crystal Rotation Axis
D	Equivalent grain diameter

3) RESULTS

3.1 Optical Microscopy Overview:

When observed under the petrographic light microscope all the present samples display a typical ureilite texture consisting of coarse-grained olivine and pyroxene texture, with the exception of NWA 7304 which is the highest shocked sample. For all samples, shock analysis was conducted in Crossed Polarized Light (XPL) and Plane Polarized Light (PPL). Olivine was observed for evident shock features such as planar fracture sets and extinction angles. The samples were also observed in Reflected Light (RL), in which Fe-O reduction rims were evident. These rims show up as opaque in PPL and XPL due to the presence of minuscule metal blebs and troilite. Presence of reduction rims are not directly pertinent to this study but they do play an intrinsic role in the big picture applications of this work.

The petrographic thin section (PTS) for NWA 11993 is predominantly composed of olivine and pigeonite grains $\leq$1mm in diameter separated by a fine-grained matrix with abundant Fe-O-rich weathering product. Metal is present in the form of small blebs evident in reflected light. Fig. 4A is a graph depicting the number of analyzed olivine grains vs. shock stage. In conclusion to the petrographic shock analysis this meteorite is represented as an S4 with a weighted shock stage of S3.5 and a standard deviation of .56. The number of olivine grains analyzed for shock stage classification was 88.

The PTS for NWA 12433 depicts a typical ureilite texture of coarse $\leq$ 1mm olivine grains. Central to the PTS is a zone of comparatively smaller grains

approximately <.5 mm. Evidence of metals is found to be present in reflected light images. The shock analysis of this specimen yielded a weighted shock stage of S4.1 .

NWA 7630 contains a moderate amount of dark opaque material in PPL. This meteorite appears to be an S3 (weighted shock stage 2.9). Olivine grains in this sample are large and depict reduction rims in reflected light. The standard deviation of the weighted shock stage is 0.66.

NWA 7304 contains an atypical texture. Olivine is present as fine grains significantly less than 1mm in diameter. This ureilite was previously classified as an S6 ureilite meteorite by A. Ruzicka and M. Hutson of the Cascadia Meteorite Laboratory as seen in Table 2. Based on results from the shock stage analysis of NWA 7304 the assertion of S6 is supported.

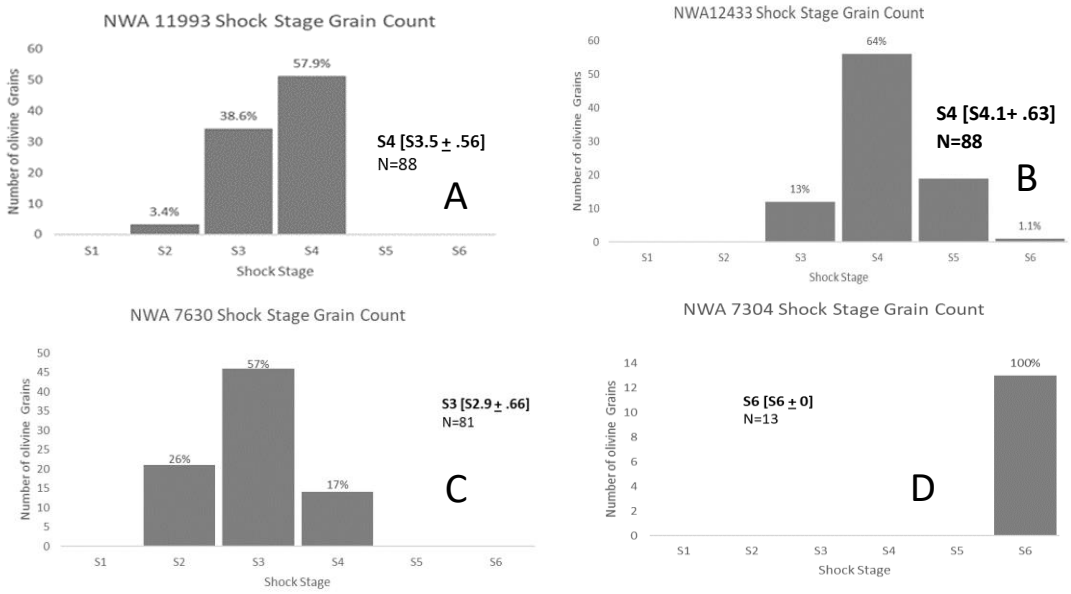

Figure 4. Shock stage histograms for NWA 11993 (A), NWA 12433 (B), NWA 7630 (C), and NWA 7304 (D). Graphs depict shock stage grain counts. The Shock stages are labeled in the X axis from 1-6 corresponding to the intensity/ frequency of identified shock features as outlined in Table 1. The Y axis portrays the number of grains with corresponding shock features. Percent of grains of a specific shock stage are present as labels above their corresponding bar and number. Weighted shock stages and standard deviations are expressed in brackets next to conventional shock stage. Number of grains analyzed is expressed as N below the listed shock stages.

3.2 Scanning Electron Microscopy:

Table 5: Modal abundance for ureilites based on large area map EBSD data

Minerals	NWA 11993			NWA 12433			NWA 7630			NWA 7304		
	Ng	Area mm^2	Area %	Ng	Area mm^2	Area %	Ng	Area mm^2	Area %	Ng	Area mm^2	Area %
olivine	4331315	108.28	81.09	3367	36.15	78.31	4350	69.53	82.35	119938	6.35	91.18
pigeonite	4881	24.39	18.26	2174	9.76	21.14	4889	14.71	17.42	16908	0.51	7.4
augite	11453	0.29	0.21	893	0.16	0.35	749	0.12	0.14	508	0	0.05
orthopyroxene	127	0.02	0.02	24	0	0.01	124	0.03	0.03	4499	0.08	1.15
troilite	316	0.06	0.05	217	0.03	0.06	124	0.03	0.03	173	0	0.03
plagioclase	27	0.04	0	1	0	0	1	0	0	1	0	0
chromite	0	0	0	1	0	0	0	0	0	2	0	0
bcc metal	7	0	0	14	0.01	0.03	0	0	0	307	0	0.04
graphite	2079	0.49	0.37	427	0.05	0.11	635	0.03	0.04	644	0	0.06
diamond	2	0	0	14	0	0	0	0	0	823	0.01	0.09
sum=	4350207	133.54	100	7132	46.16	100.01	10924	84.44	100.01	143809	6.96	100

Ng = number of indexed grains

The EBSD data provide information on mineral modes based on mineral indexed grains and these data are shown in Table 5. Overall phases in ureilites are dominated by olivine in a range of 78-91% and pigeonite from 7-21%. Other accessory phases are present including graphite in a range of .04-.37% as shown in Table 5. Graphite didn't index well in EBSD analysis and Table 5 underestimated the likely true proportion of graphite as implied by EDS maps in Fig. 6A and 6C. In Fig. 6A and 6C, for sample NWA 12433 and NWA 7630 respectively, carbon is evident interstitially as elongate crystals. Due to the crystal shape of the carbon it is most likely graphite. In NWA 11993 carbon was also present in EDS maps (Fig. 6E) However, carbon in these images did not have the same morphology as graphite in NWA 12433 and NWA 7630. Instead carbon appeared to be mounded (Fig. 6E) and could be present as a result of sample contamination from carbon coating. Graphite could have also been plucked from the PTS during polishing. Accessory minerals were found to be present in the form of diopside, troilite, and hypersthene. Other minerals are present in Fig. 5 but are not mentioned in Table 5; they were included in the list during data acquisition but initially yielded such low volumes that they did not warrant consideration in the table. Though metals do not appear to have large abundances in these meteorites their intermittent presence in optical work was noted. Data in Table 5 show more troilite than metal, and most of this troilite is in the reduction rims.

As noted in the optical petrography section samples NWA 11993, NWA 12433, and NWA 7630 are comprised of coarse grained olivine and pyroxene with grains up to ~1mm in size. This was observed as well in SEM images. Olivine and pyroxene are

also present interstitially as smaller <1mm grains. The exception to these typical ureilite textures is seen in Fig. 5B. Grains in NWA 7304 map show sharp 15^{o} boundaries with triple junctions and some interstitial fine pyroxene rims characteristic of recrystallization. There is also a single pigeonite phenocryst present in the view from which pyroxene rims appear to be propagating from along cracks. Pigeonite rims were also noted in the typical textured ureilites (Fig. 6).

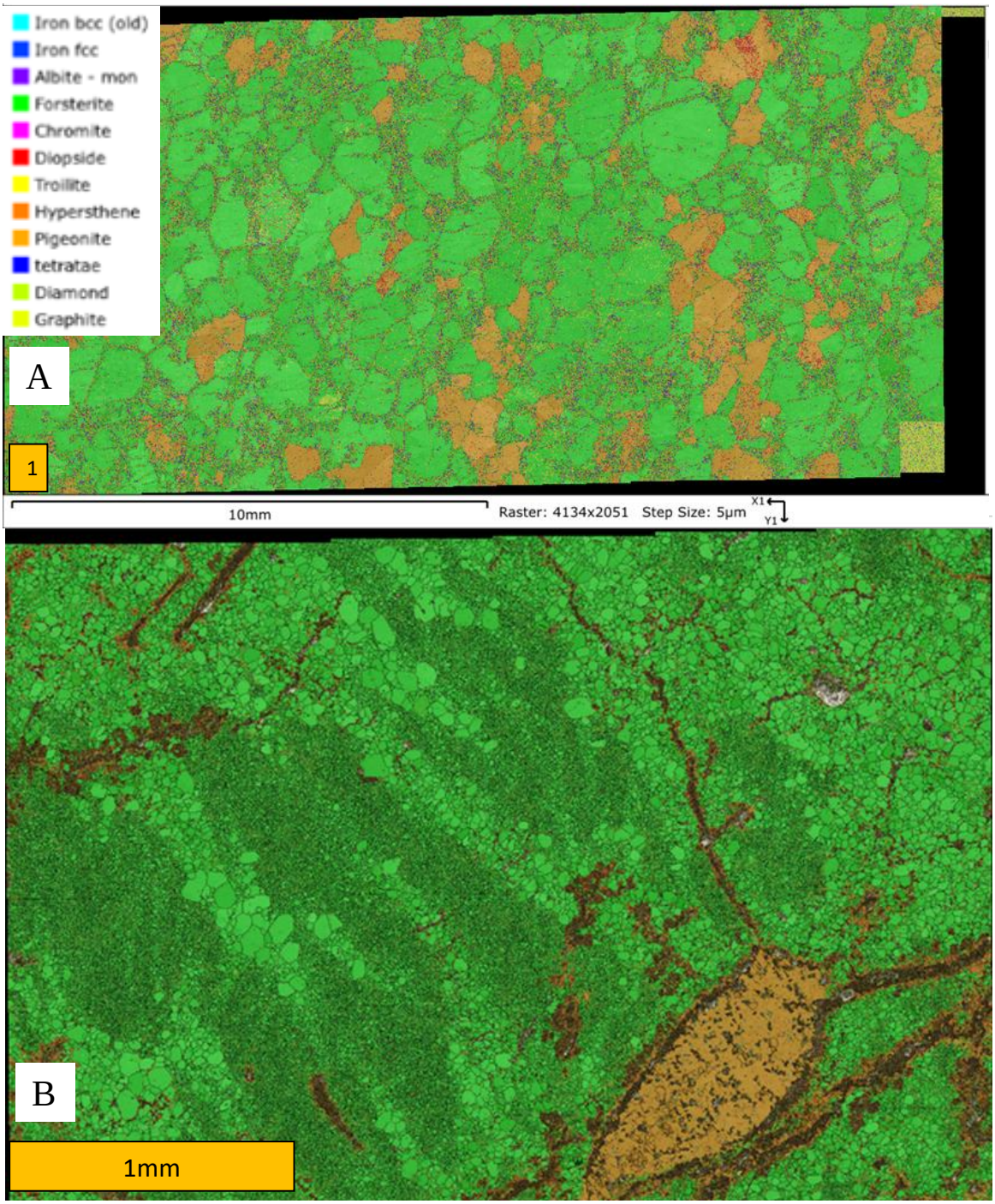

Figure 5. EBSD phase maps for NWA 11993 (A) and NWA 7304 (B). Image B) also depicts Grain Boundaries as black lines representing orientation variations >15º. This feature in (B) serves to highlight the recrystallized texture. The legend above shows the color correspondence for the identified phases. Most notably in images A-B is the abundance of forsterite (Green) and pigeonite (Orange). The orange rectangles in the maps represent 1mm scale. There were also instrumentation errors during data acquisition for the last few fields of view in NWA 11993 as can be seen in the bottom right and top right corners of map A.

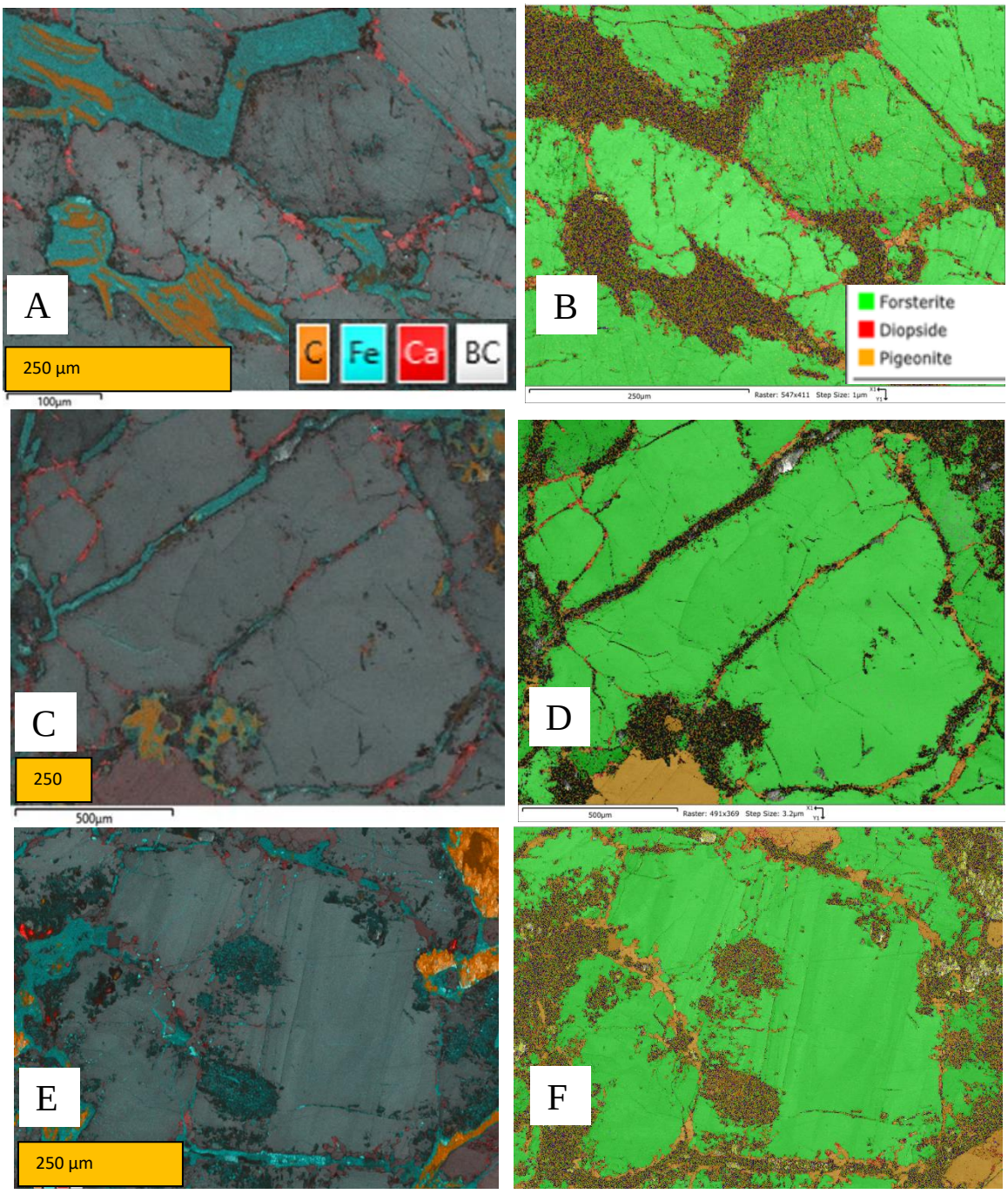

Figure 6. EDS composite element maps and EBSD phase maps for NWA 12243 (A,B), NWA 7630 (C,D), and NWA (E, F). EDS maps highlight carbon presence in the sample (Orange). Pigeonite rims form reddish areas in these images. B,D, and F are Phase maps. They depict olivine as green, pigeonite as orange, and diopside as red. Orange rectangles at the bottom of EDS maps serve as scale corresponding to 250 µm

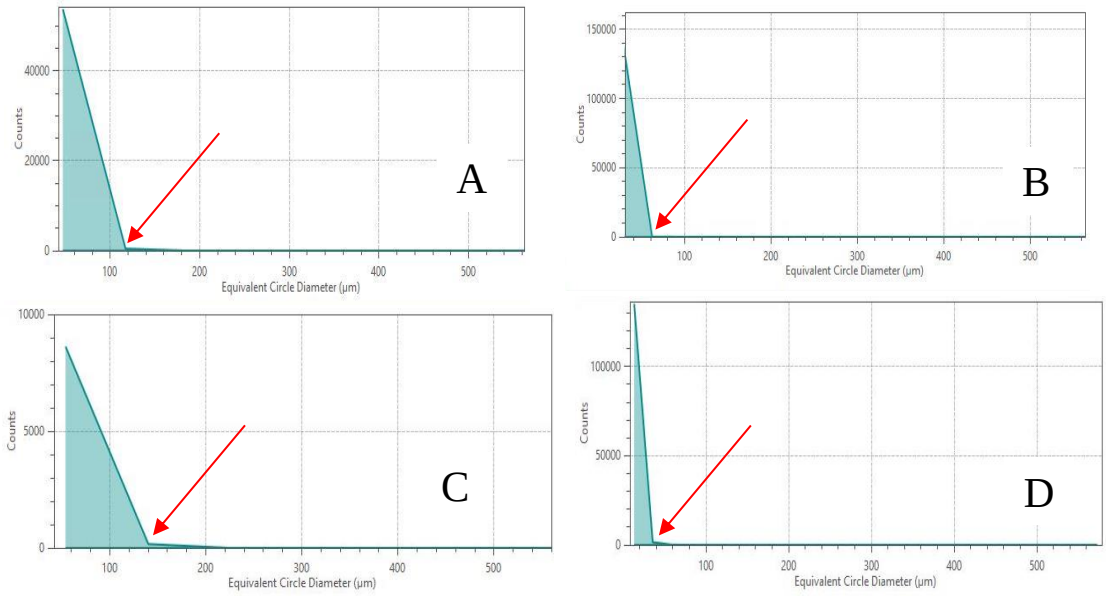

Figure 7. Grain size distributions for (A) NWA 11993, (B) NWA 12433, (C) NWA 7630, and (D) NWA 7304. Grain size is modeled as equivalent circle diameter. Inflection points are represented by the red arrow in image A-D. Inflection points are as follows: (~120, ~70, ~140, and ~15 µm) for NWA 11993, 12433, 7630, and 7304.

The EBSD data in Fig. 7 provides grain size distributions. For the LAMs, grain size distributions for olivine and pigeonite in the four ureilites have inflections at different values of d (~120, ~70, ~140, and ~15 µm) for NWA 11993, 12433, 7630, and 7304, respectively as seen in Fig. 7. These inflection points provide a convenient divide between the coarse (phenocrystic) and fine (interphenocrystic) fractions of the ureilites. One IPF map was created for each size fraction. A portion of the fine subsets' populations are derived from the reduction rims of coarse grains. This can be seen in the Inverse Pole Figure (IPF) target maps of Fig. 8 below. The colors of grains in Fig. 8 depict grain orientations. Grains with similar colors are portraying similar orientations. In the coarse and fine images, the two-color boxes indicate an area where the coarse grain

and surrounding fine grains in the reduction rim have the same orientation. Furthermore, all of the individual grains in this area are indexing uniformly as well. That is to say, Band Contrast (BC) is the same, and so similar indexing quality and similar orientation both suggests the disconnected grains are actually the same.

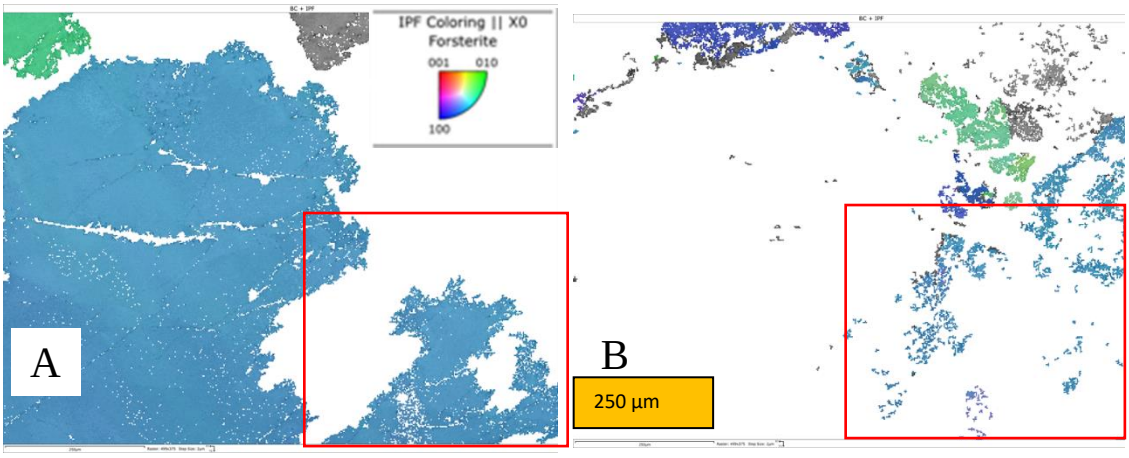

Figure 8. EBSD Inverse pole figure (IPF) target area maps for coarse (A) and fine (B) subsets in sample NWA 11993. The red boxes highlight the areas of interest comparing coarse and fine subsets. The orange rectangle in the Lower corner of B) represents a 250 µm scale for both images. Forsterite coloring for the X view is presented at the top of image A).

Essentially the deformation features within the rims are being compared to deformation within the phenocrysts. The fine-grained subset is not exclusively comprised of reduction rims, and there are still interstitial grains in the fine subset that are independent of the phenocrysts. The KAM deformation map in Fig. 9 depicts the variable deformation in typical ureilites NWA 12433 and NWA 11993. Higher deformation is seen at the edges of grains and within grains along kink bands. This is further emphasized with Fig. 9B and 9C showing coarse and fine grains respectively. The high deformation

edges and interstitial areas indicate that the processes associated with reduction helped create some deformation.

Within the coarse grain in Fig. 9B, the lamellar green features indicate misorientation. These coincide with subgrain boundaries. Deformation is preserved disparately between coarse and fine grain fractions for the first three samples, as well as

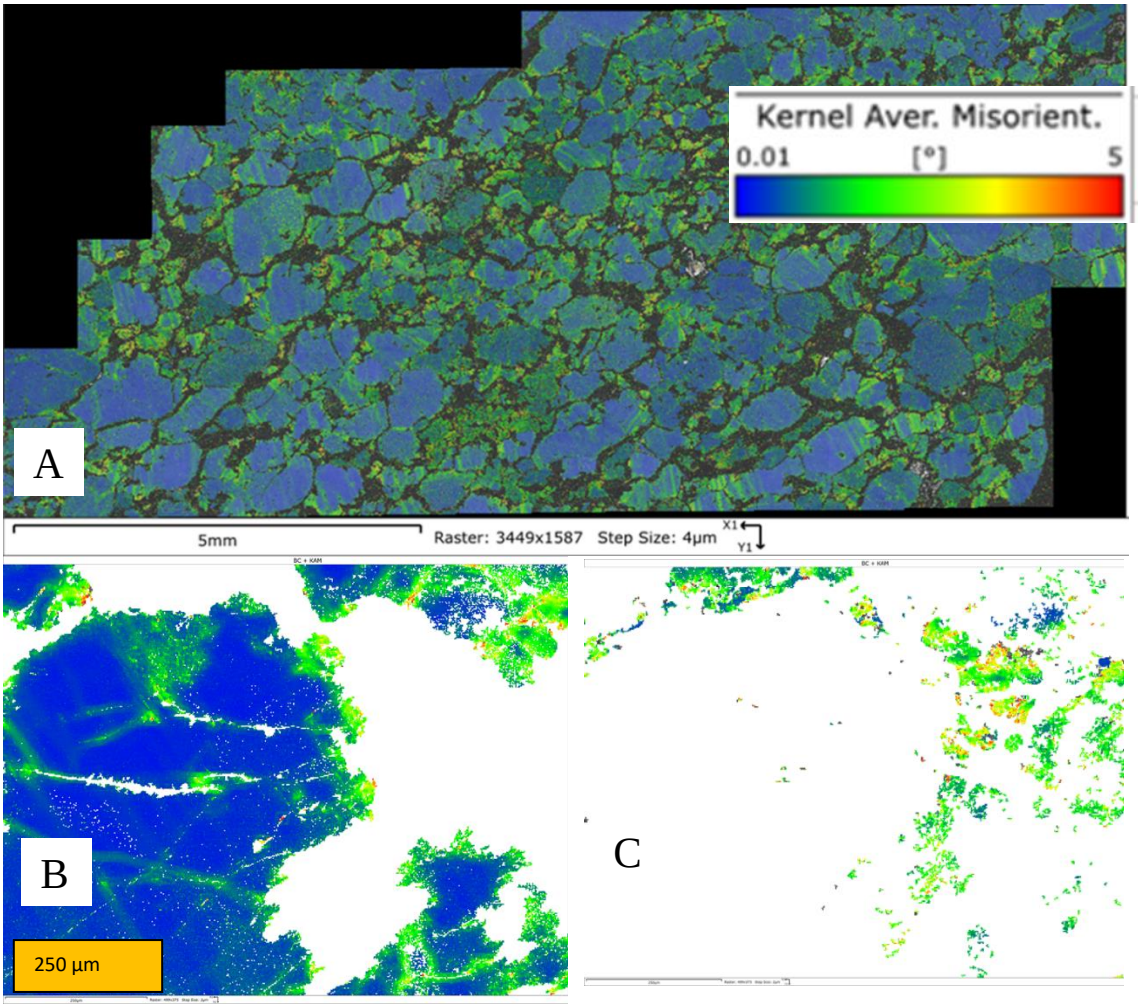

Figure 9. Composite EBSD Kernel Average Misorientation (KAM) maps for NWA 12433 (A), and NWA 11993 (B,C). Image A) is a large area map. Images B) and C) portray targeted area maps (TM1) for coarse (B) and fine (C) subsets for sample NWA 11993. The scale for B and C is represented by the orange rectangle in (B) which corresponds to 250 µm.

in the rims of larger grains. This can be seen in Fig. 9. Coarser grains have lower KAM values for phenocrysts overall compared to the finer-grained edges of the grains (Fig. 9). The variability between deformation in large grains and small grains is present in Fig. 9 in which edges and interstitial grains are retaining high deformation values.

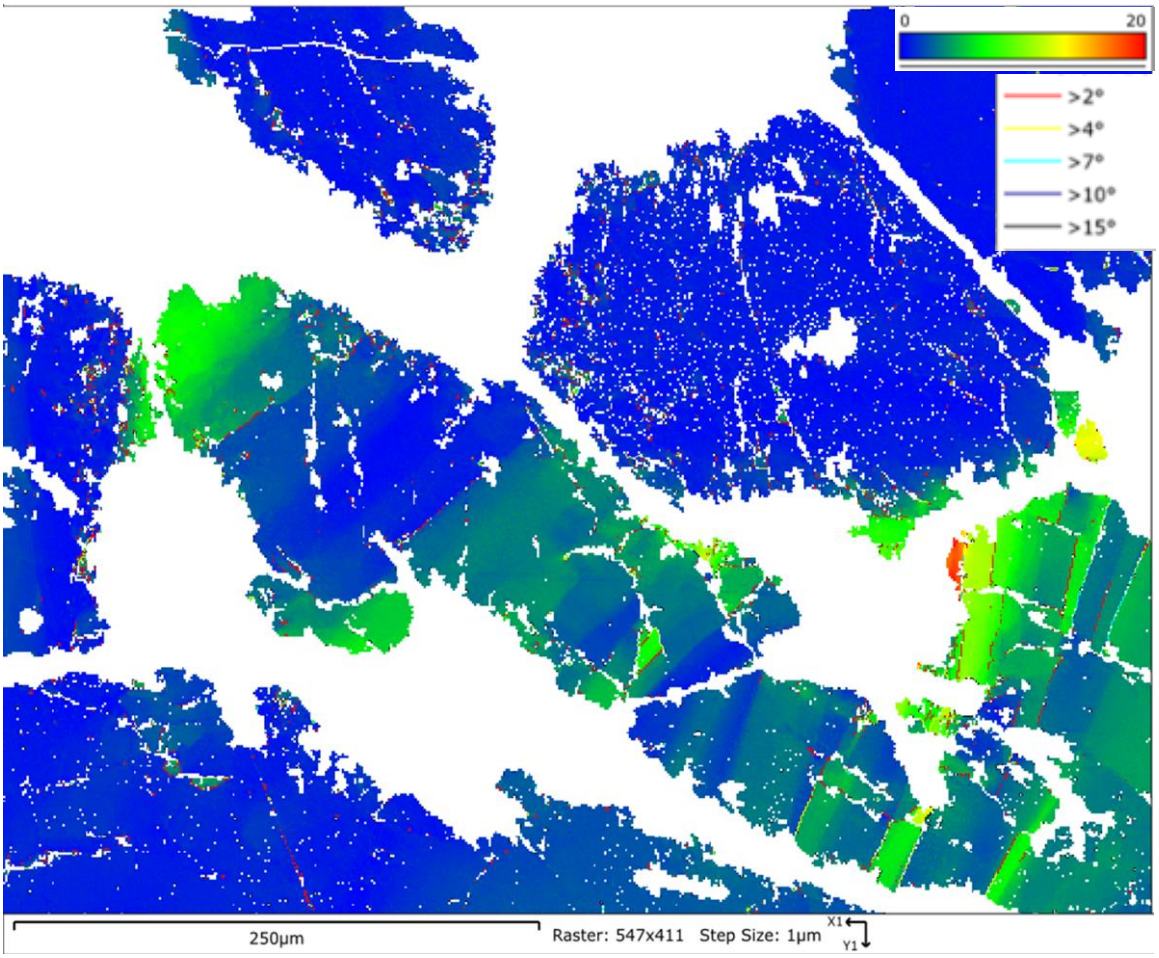

Figure 10. Grain Reference Orientation Deviation Angle (GROD-Ang) target map for NWA 12433 (TM5). GROD-ang legend is expressed in the top right corner of the image as a color coordinated range of 0-20º. Subgrain boundaries are present and color defined in the legend with correlated angles > 2, > 4, >7, > 10. Grain boundaries are present as >15º.

Fig. 10 is another deformation map that emphasizes the relationship of the subgrain boundaries bordering the green misorientations. The subgrain boundaries in Fig. 10 correspond to the 2-10 º rotations which serves as the range for the CRA diagrams in

Fig 12. Furthermore, the lines are associated with the SB or special boundaries as characterized in Fig. 11.

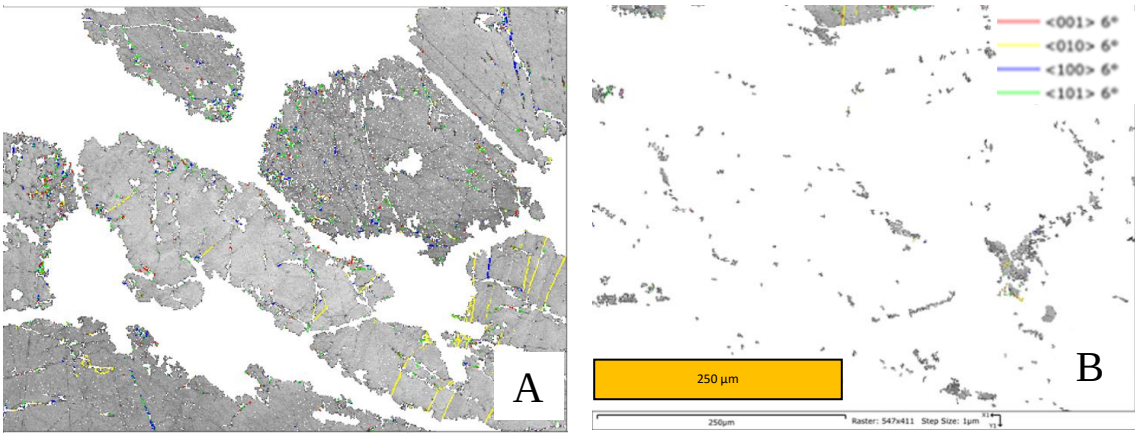

Figure 11. EBSD Special Boundary (SB) targeted area maps (TM5) of the coarse (A) and fine (B) grains subset for NWA 12433. These images depict Band Contrast (BC) and Special Boundary (SB) map layers. The SBs for the maps are color coordinated to represent different Crystal Rotation Axes CRAs as defined in the legend in image B. The monochrome band contrast layer represents olivine grains in which the SBs are found. The scale is represented by the orange rectangle in the bottom of image B which corresponds to 250 µm.

The special boundaries as depicted in these maps correspond to subgrain boundaries as well. However, in this map the colored lines are associated with the misorientation rotation directions. The prevalent <010> (yellow) subgrain boundaries as seen in Fig.11 were found in all samples. In phenocrysts they are present as long traces that correspond to kink or twist boundaries as well as major changes in orientation as seen in green lamellar features of the GROD-Ang map in Fig. 10. The subgrain boundaries in Fig. 11 also coordinate with the CRA diagrams (Fig. 12) which serve as the basis for the thermal parameter. That is, the maps in Fig. 10 and Fig. 11 visually show

where the rotations boundaries are, providing spatial context. The CRA diagrams (Fig. 12) present quantitative representations for the rotation axes in the form of MUD values.

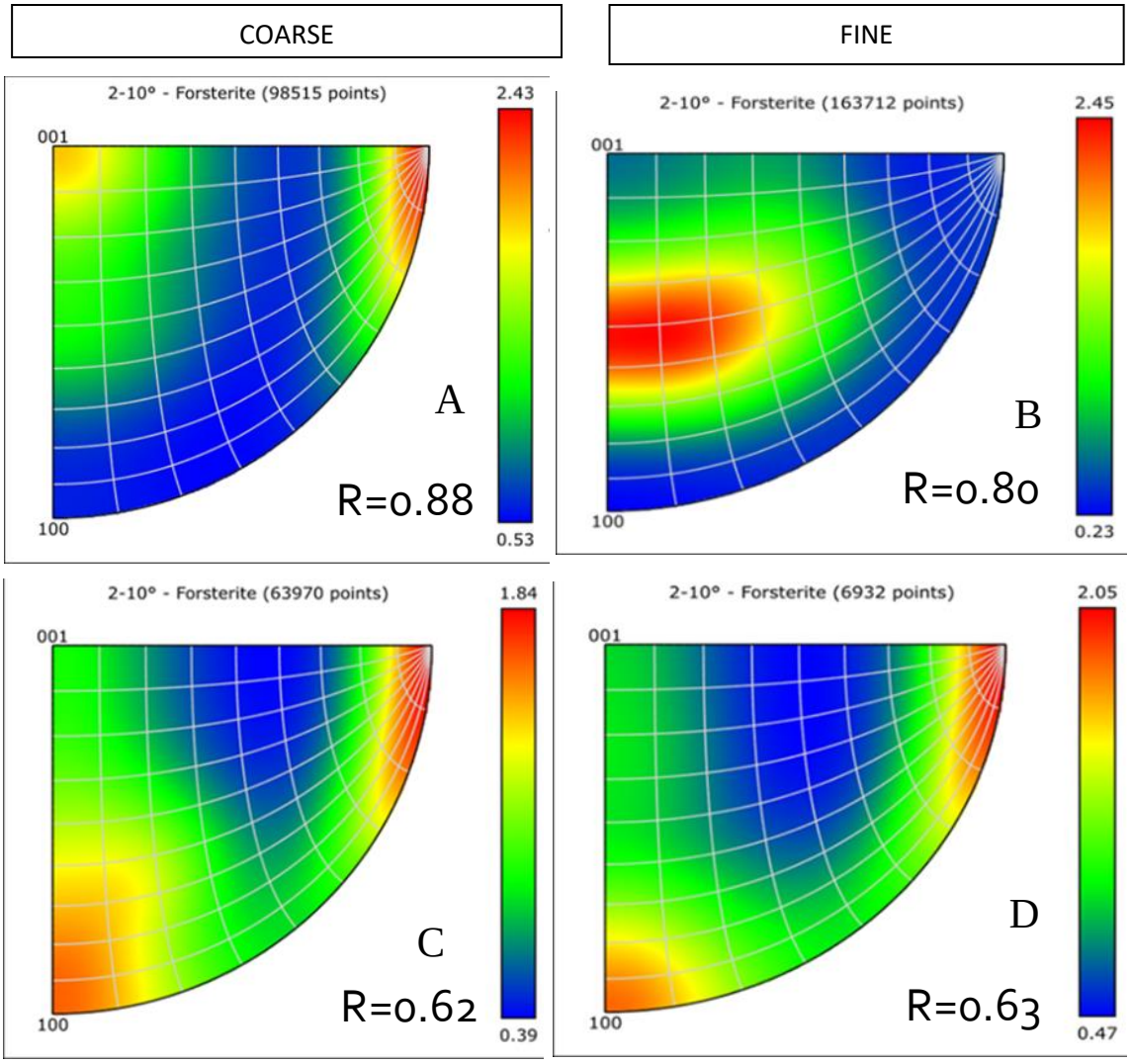

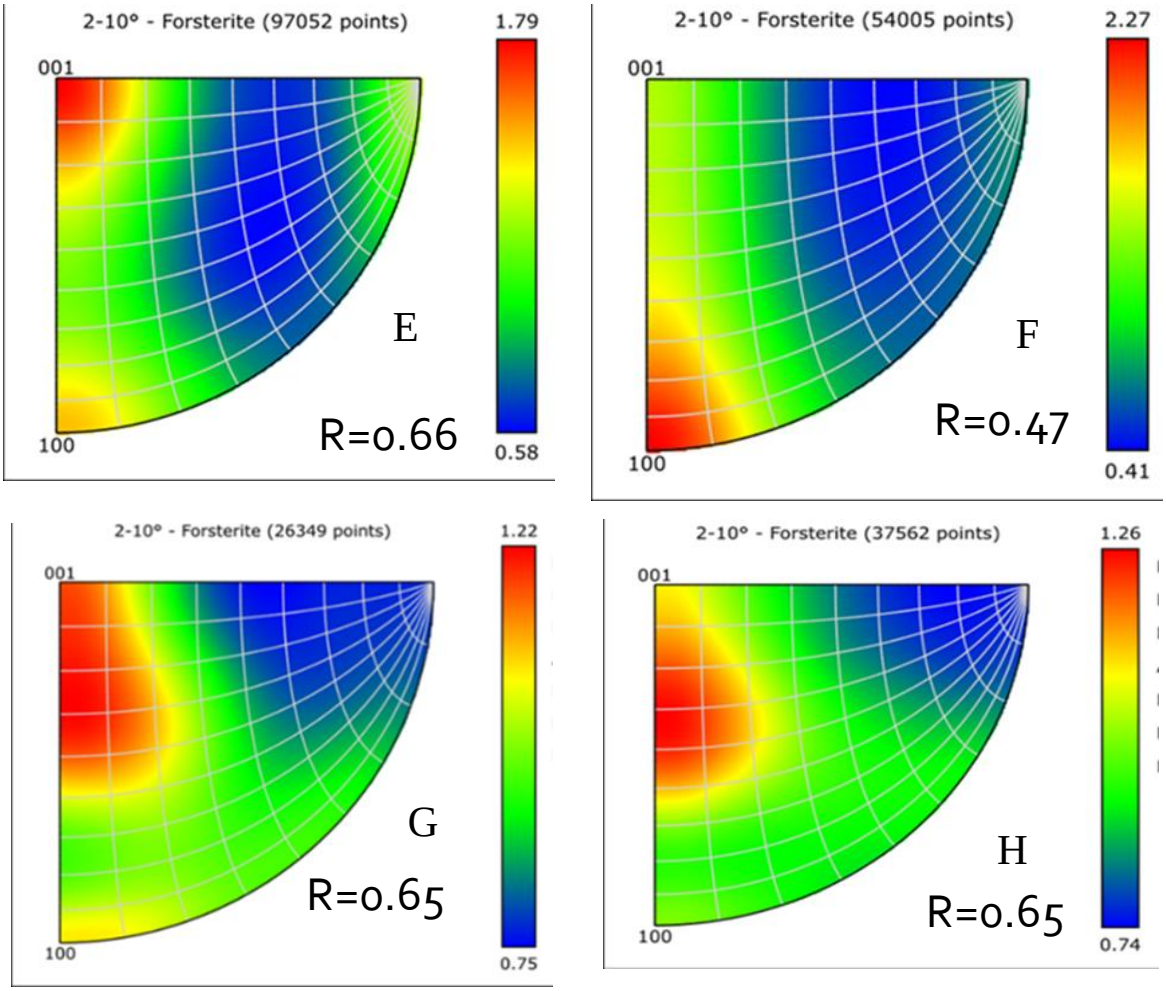

Figure 12. Crystal Rotation Axes (CRA) diagrams of 2-10º rotations for NWA 11993 (A,B), NWA 12433 (C,D), NWA 7603 (E,F), and NWA 7304 (G,H). Coarse grains subsets are present in the left column and fine grains subsets are expressed in the right. Multiples of Uniform Density values are color coded with low populations being blue and high being red, as seen in the corresponding legends for each diagram. Calculated R values are portrayed in the lower right corner of each diagram.

Overall values are concentrated in the “warm” <010> and “hot” <001> associated slip directions (Fig. 12). Though there are some exceptions, C and D have secondary peaks in the “cool” <100> rotations. F has the most concentrations in the cool rotations. The “warm” rotation directions are common in phenocrysts of all typical texture ureilite samples. <010> rotations are also present in fine grains of typical texture ureilites; however, due to the small size of the grains and the small amount of pixels in such grains, the special boundaries (SBs) are difficult to see. MUD values were identified and placed into a table to measure the fraction of crystal rotation axes values. The resulting R metric found for 2-10^{o} can be found in the bottom right corners of the associated diagrams. NWA 11993 coarse grains depicted highest MUD concentrations in the <010> directions. Calculated R values are .88 and.80 for coarse and fine subsets respectively. In NWA 12433 the MUD values are concentrated in the <010> with secondary peaks present in the <100> for both coarse and fine grain subsets. Calculated R values for both subsets yielded R values of .62 and .63 respectively.

In NWA 12433 the coarse subset presents MUD concentration in the <001> directions with a secondary peak in the <100> field. The fine subsets house higher concentrations in the <100>. $R_{2\text{-}10}$ values for the coarse and fine subsets are .66 and .64 respectively. The lowest R values from this study are derived from the fine fraction of NWA 7630. MUD values for coarse and fine grain subsets for NWA 7304 yielded identical $R_{2\text{-}10}$ values of .65.

With the exception of NWA 11993, and the fine subset for NWA 7630, the $R_{2\text{-}10}$ values are present in a range from R= .62- .66.

COARSE	FINE

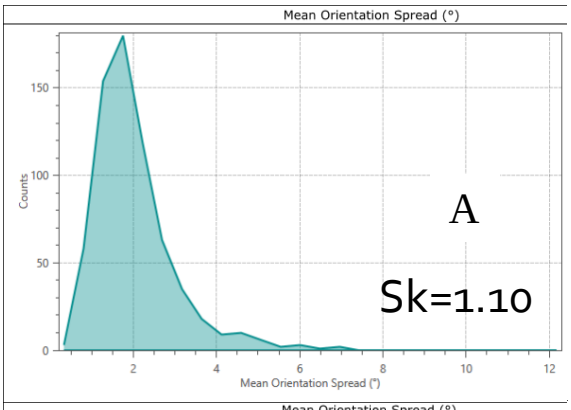

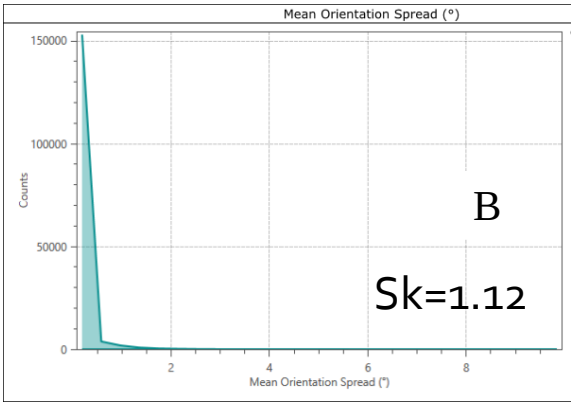

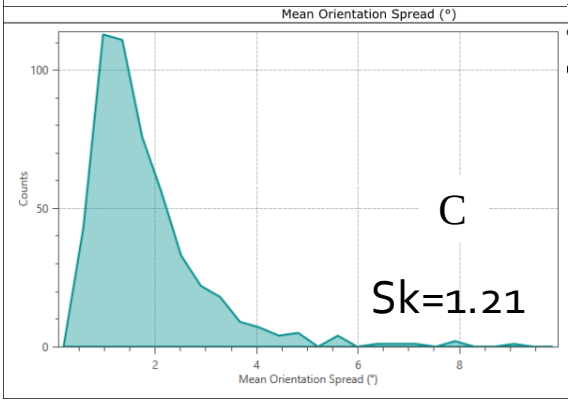

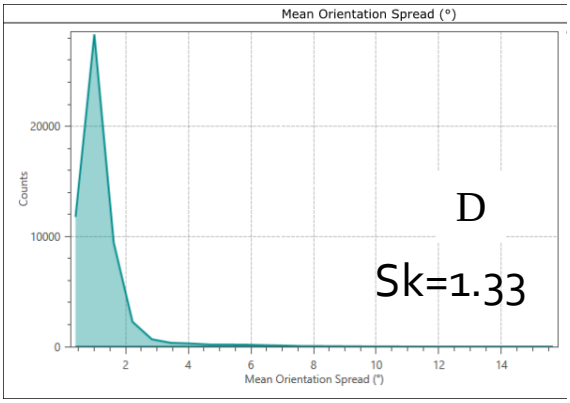

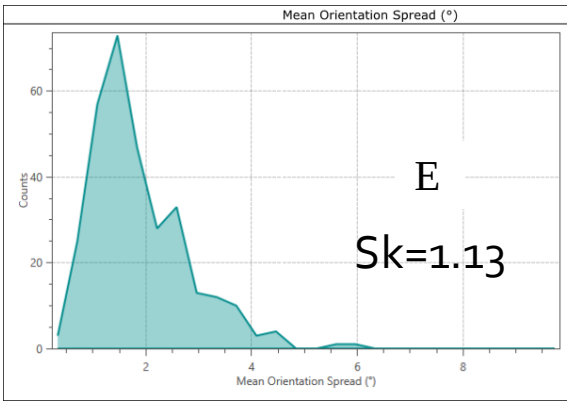

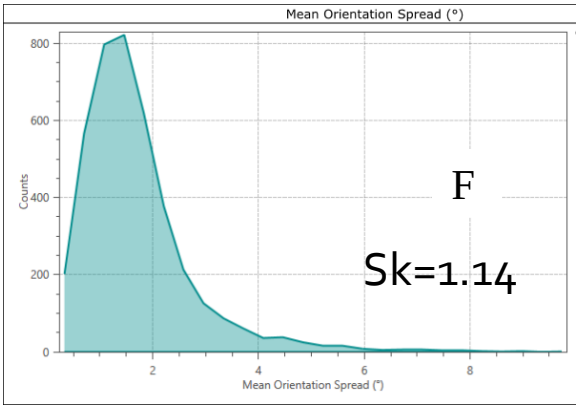

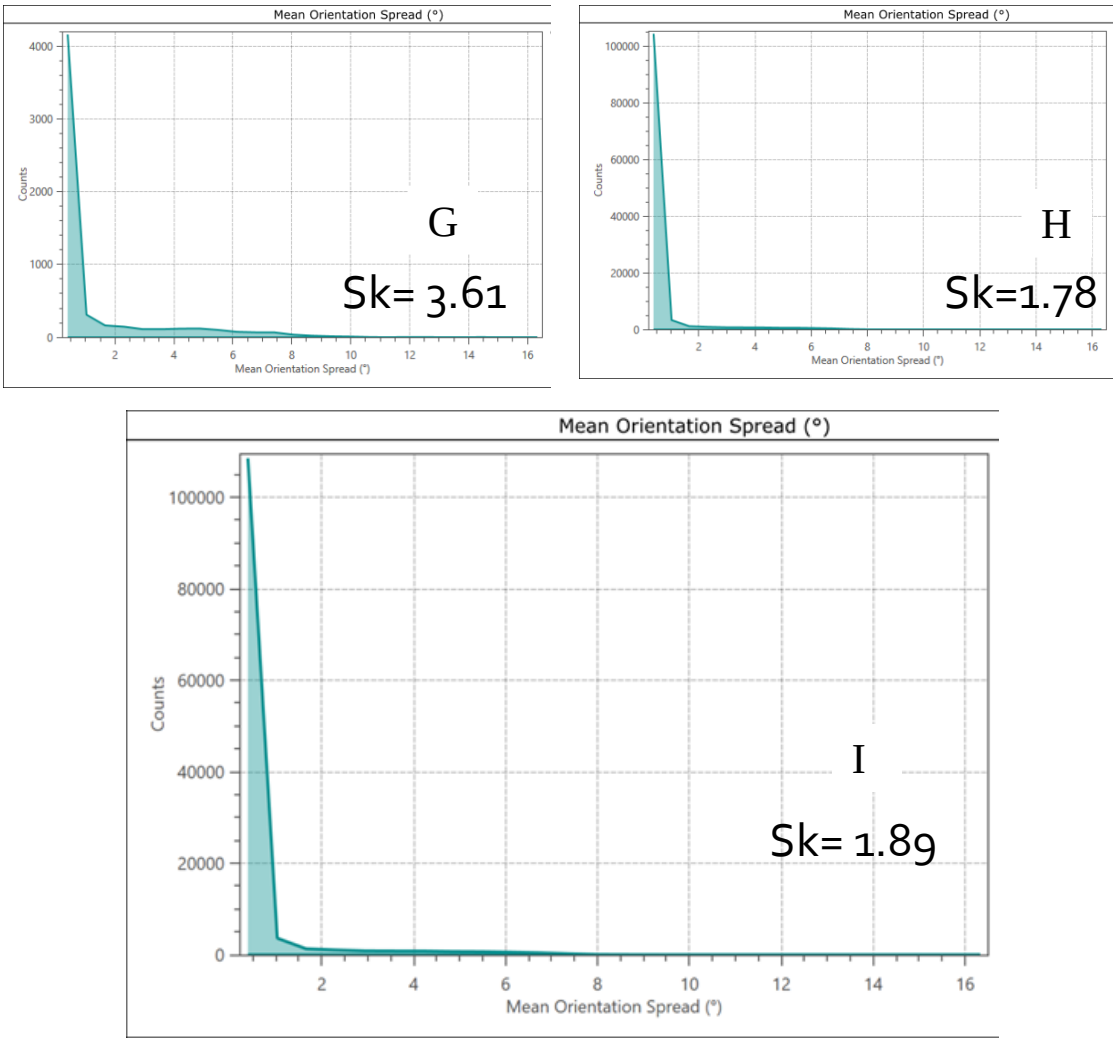

Figure 13. Mean Grain Orientation Spread charts for NWA 11993 (A,B), NWA 12433 (C,D), NWA 7630 (E,F), and NWA 7304 (G,H,I). GOS for the coarse grains are in the left column and GOS for the fine grains are in the right column. The calculated skew (annealing parameter) is expressed in the bottom right corners for each chart. Image I is a GOS chart for olivine grains of all equivalent circle diameter

GOS values in Fig. 13 present overall low-moderate values (mostly ~1-3°) for grains in the typical textured ureilites NWA 11993, NWA 12433, and NWA 7630 (Fig. 13A-F). The GOS distributions for these meteorites are relatively symmetric, resulting in modest Sk values (Fig. 13A-F). NWA 7304 is different, with most grains having low GOS (<1°) but with some grains having high GOS, giving an asymmetric distribution

with high Sk values (Fig. 13G, Fig. 13H, Fig. 13I). The cumulative subset data for the thermal and annealing parameters are expressed below in Table 5. Also shown in table 5 are mean GOS values ± the standard deviation. As seen in Fig 13 and Table 5, the mean GOS value for the coarse grains in NWA 7304 is similar to the typical ureilites, but the fine grains and all grains subset for this meteorite yield mean GOS values significantly lower than any other sample.

Table 6: EBSD parameter data for four ureilites

Meteorite	Subsets (um)	GOS Mean± S.D	Sk	R2-10
NWA 11993	D>120	1.95 ± 0.95	1.1	0.88
	D<120	1.13 ± 0.64	1.12	0.80
NWA 12433	D>70	1.80 ± 1.09	1.21	0.62
	D<70	1.19 ± 1.00	1.33	0.63
NWA 7630	D>140	1.96 ± 0.98	1.13	0.66
	D<140	1.66 ± 1.05	1.14	0.47
NWA 7304	D>15	1.23 ± 1.98	3.61	0.65
	D<15	0.53 ± 0.95	1.78	0.65
	All D	0.57 ± 1.03	1.89	0.65

The ureilite subset data as seen in Table 6 was plotted with type 6 chondrite data from Ruzicka and Hugo (2018). In Fig. 14 low and high values for GOS, $R_{2\text{-}10}$ (thermal parameter), and Sk (annealing parameter) are compared with chondritic benchmarks present in the following ranges: GOS= .63- 4.5, $R_{2\text{-}10}$= .35-.80, and Sk=0.99 - 2.27. The R

value for the coarse grains subset of NWA 11993 at .88 is higher than the previous chondrite derived benchmark and thus now serves as the high marker for R values.

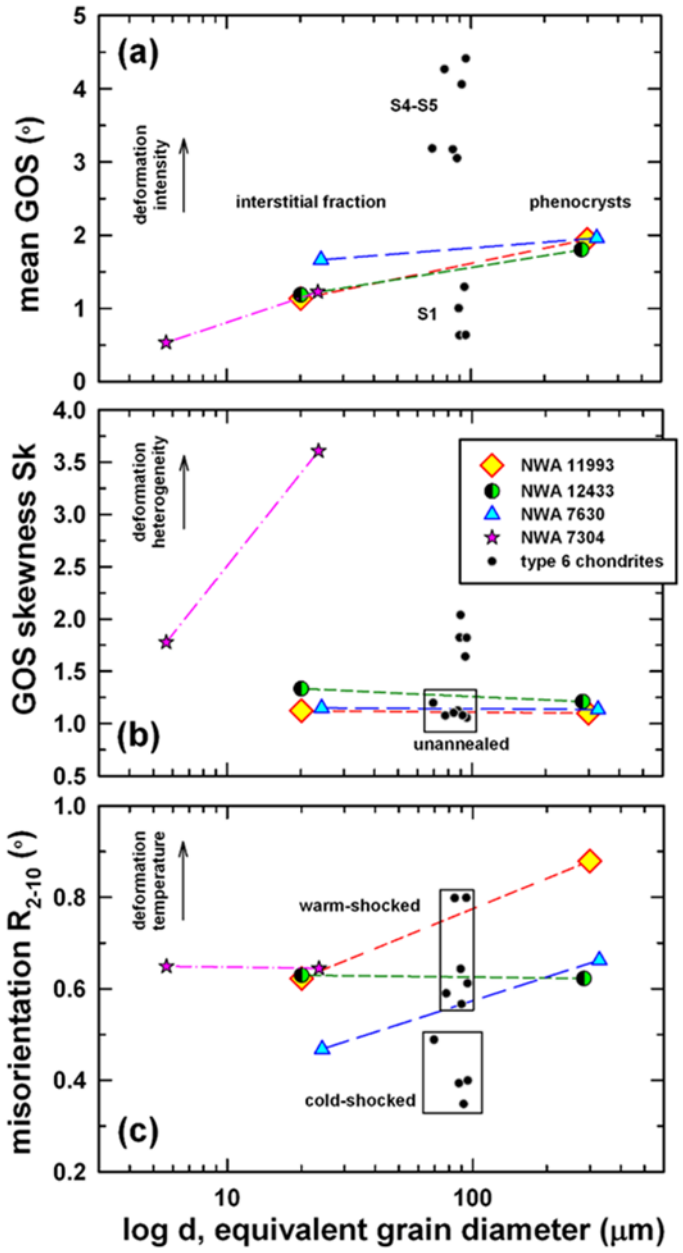

Figure 14. Chart was acquired from Frye and Ruzicka2022. EBSD-derived metrics for GOS, Skew, and $R_{2\text{-}10}$ (large area map data) for olivine in the coarse and fine fractions of four ureilites compared to type 6 ordinary chondrites data from Ruzicka and Hugo 2018.

4) DISCUSSION

4.1 Phases:

Pigeonite in the samples tells a story regarding the reduction of FeO in the rims of olivine grains. Pigeonite phases are present around olivine in a rim-like fashion and appear to be associated with FeO- reduction rims as seen in Fig.6. Pigeonite rims were found in all the analyzed ureilites. In locations where they are especially abundant it appears to corrode into olivine grains. The reaction is fueled by interstitial graphite which reduces Fe-O in olivine leaving behind metal blebs and CO gas (Goodrich et al.,2004).

For NWA 7304, Fig. 15C and 15D indicate that reduction happened prior to deformation. This point for NWA 7304 is further emphasized in Fig. 16 which shows an Inverse Pole Figure map for the sample. Figure 16 in tandem with Figure 15B and 15C show that the Mg-rich reduced areas consist of the same type of small grains as non-reduced areas.

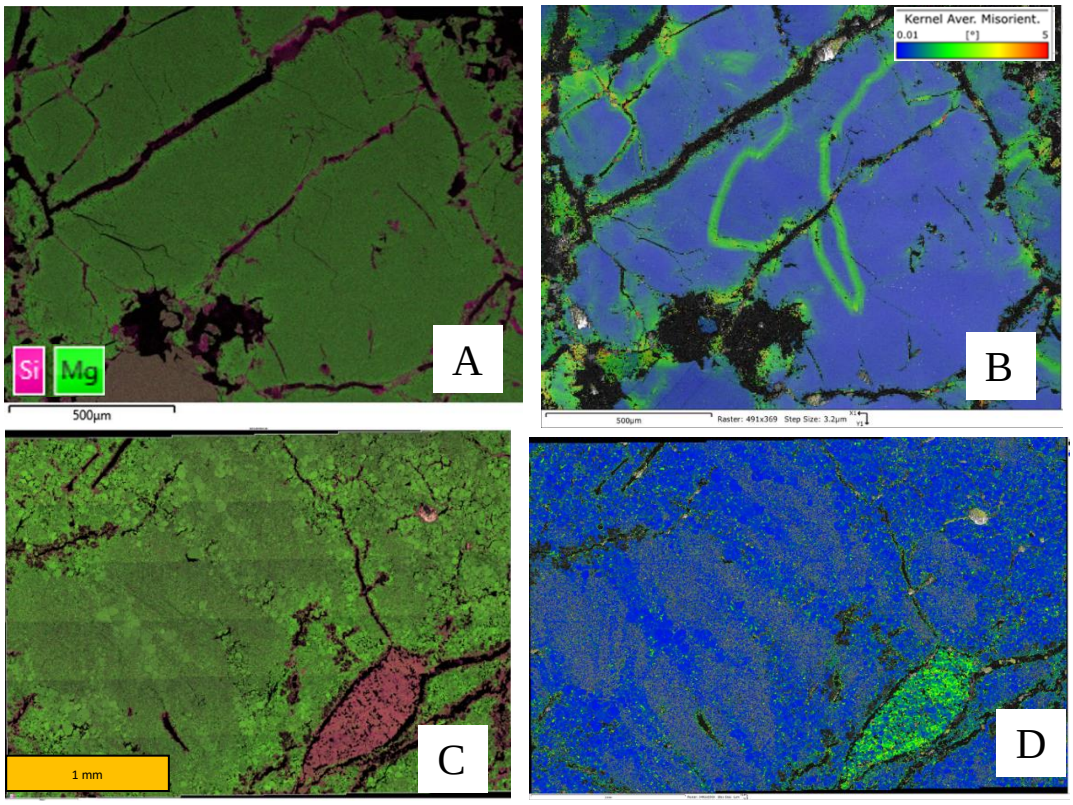

Figure 15. Composite EDS and EBSD maps for NWA 7630 (A,B) and NWA 7304 (C,D). A) and C) are EDS Si+Mg maps which highlight Mg enrichment (brighter green color) and presence of Si-rich material (pink) and pigeonite (brown-red) in rims and along crack-like features that underwent FeO-reduction of olivine. C) and D) are KAM maps depicting the relative deformation of both samples in comparison to reduction rims. Scales for these maps are represented by the orange rectangles at the bottom of B and D corresponding to 1 mm. Legend for the KAM is expressed in the top corner of image B.

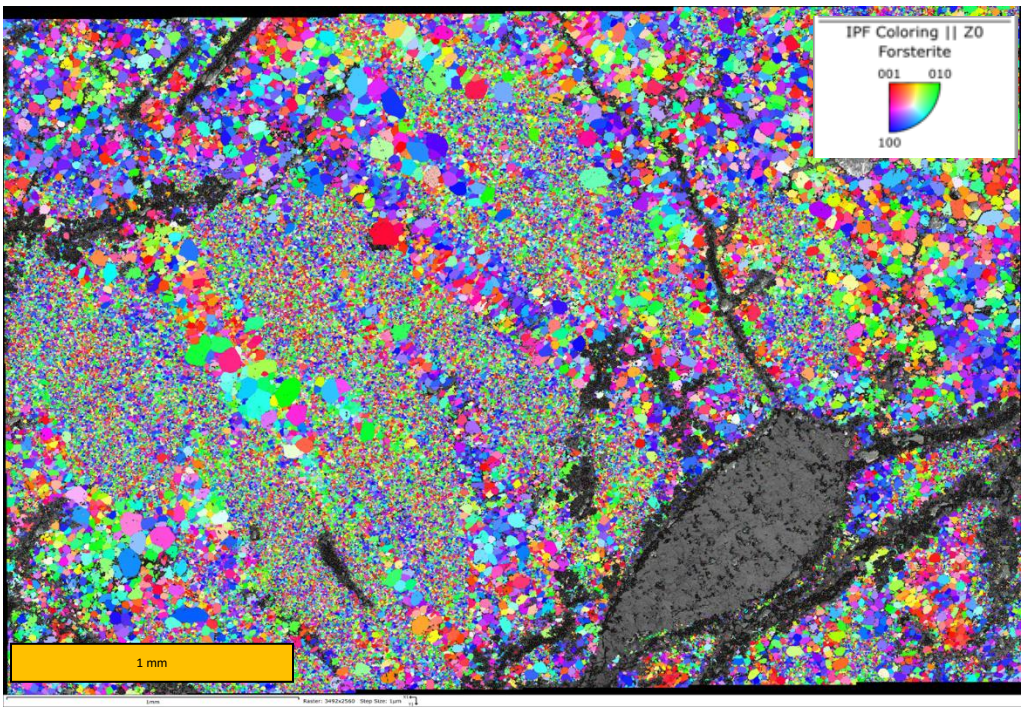

Figure 16. EBSD Inverse Pole Figure (IPF) large area map for olivine in NWA 7304. This figure depicts the relative orientations of olivine grains in the Z view. Scale is expressed in the bottom of the image by an orange rectangle that corresponds to 1mm. The IPF legend is present in the top right corner of the figure.

For NWA 7630, in contrast, there is evidence that deformation within phenocrysts happened prior to reduction of the olivine rims. This can be seen from the crack-like reduction area in Fig 15B that cross-cuts the curvilinear deformation feature (subgrain boundary with <010> rotation misorientation) in the large grain (Fig. 15A, Fig. 17). When compared to reduction rims in Fig 15A it appears that reduction in NWA 7630 happened after the subgrain boundary with the <010> rotation misorientation formed. Features in the other ureilites were more difficult to study as they did not have such evident relationships between deformation and reduction. However, based on the two samples

presented in Fig. 15 it can be said with confidence that ureilites can have different deformation histories.

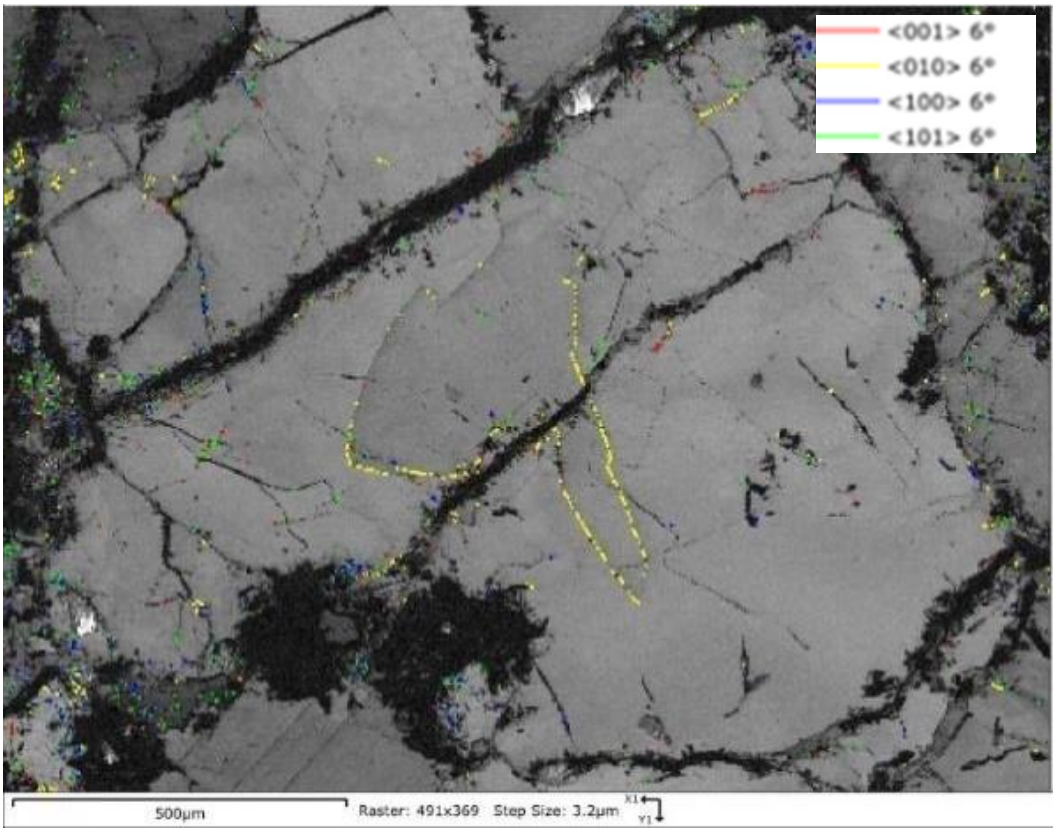

Figure 17. EBSD Special boundary (SB) and Band Contrast (BC) targeted area (TM5) map of NWA 7630. The SB layer emphasizes the rotation axis of the central deformation feature. The SB legend is depicted in the top right corner of the figure.

4.2 Disruption While Hot:

Table 7: $R_{2\text{-}10}$ Large Area Map subset data and associated model temperatures as calculated using the method of Ruzicka and Hugo (2022)

Meteorite	Subsets (μm)	$R_{2\text{-}10}$	Temp ^{o}C
NWA 11993	D>120	0.879	1224±75
	D<120	0.803	1141±79
NWA 12433	D>70	0.622	946±88
	D<70	0.629	938±89
NWA 7630	D>140	0.662	998±86
	D<140	0.468	802±95
NWA 7304	D>15	0.645	968±87
	D<15	0.649	973±87
	All D	0.539	853 ± 93

Regarding the hot disruption model of the ureilite parent body we can see in Table 7 model temperatures derived from Ruzicka and Hugo (2022). The model temperatures these authors derived were based in part on the data for NWA 11993 assuming that the deformation temperature was ~1225 °C, the best estimate for mantle equilibration temperature taking into account the composition of olivine and pigeonite grain cores in this meteorite (Ruzicka and Hugo, 2022; A. Ruzicka personal communication). The model temperatures assume that only temperature is important in affecting the R values. If this assumption is not met, the deformation temperatures will not be accurate.

Subset results from this study would seem to indicate that deformation happened at elevated, but not magmatic, temperatures for NWA 12433, NWA 7630 and NWA 7304, with the only truly magmatic temperatures being related to NWA 11993. This is an interesting and noteworthy feature concerning the variability of R values for the ureilites because compositionally, they are similar, and if Mg#s are a good indicator of formation depth and location (Goodrich et al., 2004), then we would expect their thermal signatures

to be the same. This is a major discrepancy that needs to be resolved in order for the hypothesis to be supported.

It was mentioned previously in this work that water content can play a role in which slip systems become active during deformation. More specifically, elevated water content in olivine leads to the production of more c- type slip (Karato et al., 2008). More c-type slip would yield lower R values.

Langendam et al., 2021 present evidence that FeO-reduction could have been fueled by percolation of CHOS fluid/gas that contained a water component. If these CHOS fluids behave similar to water when influencing olivine slip systems, then R values produced would be lower though not as a result of a comparatively cooler thermal environment. This could explain why R values are magmatic for NWA 11993 but not for NWA 12433 and NWA 7630. The percolation of this gas/fluid would be heterogenous (Langendam et al., 2021). Such heterogenous fluid action could explain why R values tend to be variable, and if the fluids were concentrated in the finer-grained interphenocryst areas, it could explain why R values tend to be lower there than within grain cores as observed for both NWA 11993 and NWA 7630 (Table 6).

Other evidence was obtained that suggests that high magmatic temperatures might be characteristic for the three normal-textured ureilites. As previously noted, <010> rotation misorientations, which are characteristic of elevated deformation temperature (Ruzicka and Hugo, 2018), are the main type of subgrain boundary found within the phenocrysts of not only NWA 11993 but also NWA 12433 and NWA 7630. The <010> subgrain boundaries tend to form long subgrain boundaries within phenocrysts whereas

other rotation types including <100> (characteristic of c-type slip) are present as short boundaries at the edges of phenocrysts. This suggests that different slip systems are recorded at grain edges compared to grain cores, with the latter having less c-slip, and grain edges more c-slip. These data suggest a model where the competing effects of temperature and fluids heterogeneously affected slip system activity in olivine in ureilites. If the CHOS fluids partly regulated slip activity in olivine in the way described, deformation temperatures in Table 7 would be lower limits for the coarse fraction in NWA 12433 and NWA 7630, and for the fine fraction of these two meteorites and for NWA 11993.

As noted in the results section, shock features for NWA 7304 make it evident that this meteorite has been heavily shocked at high temperature to the point of extensive recrystallization. This recrystallization is probably the reason behind high skew values (Table 6). For the most part deformation gets "wiped out" as the result of grain nucleation and growth within the deformed "parent" grain, however some of the coarse grains in this subset retained some deformation which resulted in the high comparative Sk values. This is different than annealing however, as this process can happen quickly and is not dependent on a slow cooling rate. Many deformation features such as subgrain boundaries were lost when the specimen was recrystallized. The slip systems that remained active yield lower R values. This is possible if the specimen was overprinted/influenced by another shock event (Ruzicka and Hugo, 2022) or if CHOS was active in the system as a fluid.

4.3 Post shock cooling:

Ureilite cooling rates that were discovered in the results of this analysis were fairly conclusive and suggest a quick rate of cooling. Skew for all three typical textured ureilites (Table 6) was fairly low indicating little annealing took place. This is indicative of fast cooling. For NWA 7304 the coarse grain subset yielded a very high skewness value. When the data was calculated again using all equivalent circle diameter, skewness was lower than the coarse grain subset and closer in value to the fine grain subset Sk. The recalculated Sk value for NWA 7304 is still high. This high Sk value is due to recrystallization though and not a result of post shock annealing.

5) CONCLUSION

Thermal parameters were calculated for four ureilite samples and found to be warm-hot in LAM CRA diagrams and statistics for coarse and fine subsets yielded a range of $R_{2\text{-}10}$ of .42-.88, which corresponds to model deformation temperatures of 802-1224 ^{o} C. Despite compositional similarity of the ureilites that were studied, R values were much more variable than expected. However, this variability is possible if CHOS fluids percolated through the Ureilite Parent Body (UPB) acting as water on the slip systems. This supports the hypothesis that meteorites were disrupted while hot within the range of 1200-1300 ^{o}C. However, our original hypothesis assumed a very low water content in the ureilite samples and that temperature would by the primary determinant. If CHOS fluids affected slip activity, R values depend both on it as well as temperature during deformation.

For the three typical textured ureilites GOS skewness (Sk) values indicated that annealing did not occur extensively and thus cooling was done quickly. For NWA 7304, which is extensively recrystallized, high Sk values are probably the result of intense shock deformation and not annealing. These results are in support of the hypothesis.

Results from this study implies slip system activation is nuanced and can be impacted by a plethora of other factors in order to yield the features we find in ureilites. Further investigations are necessary to better understand the slip systems of olivine in achondrites. This can be done by looking at deformation more closely using TEM techniques, better constraining the relationship between graphite and $R_{2\text{-}10}$ values in olivine, and reevaluating the role of fluids. One way to test the role of fluids is by

conducting analysis on ureilites that have had temperatures constrained in past studies like the ones mentioned in the introduction.

References

Barbaro, A., Domeneghetti, M. C., Goodrich, C. A., Meneghetti, M., Litti, L., Fioretti, A. M., Jenniskens, P., Shaddad, M. H., and Nestola, F. (2020) Graphite-Based Geothermometry on Almahata Sitta Ureilitic Meteorites. *Minerals 10*, 1005:doi:10.3390/min10111005

Berkley, J. L., Taylor, G. J., and Keil, K. (1980) The Nature and Origin of Ureilites. *Geochemica et Cosmochimica Acta* Vol.44, pp. 1579-1597. Department of Mineral Sciences, American Museum of Natural History. New York. NY 10024.

Brewer, L. N., Field, D. P., and Merriman, C. C. (2009) 'Mapping and Assessing Plastic Deformation Using EBSD' in Shwartz A.J., et Al. *Electron Backscatter Diffraction in Materials Science,* Springer Science+ Business Media. DOI 10.1007/978-0-387-88136-2_18,

Burbine, T.H., McCoy, T.J., Meibom, A., Gladman B., and Keil, K. (2002) 'Meteoric Parent Bodies: Their Number and Identification' in Bottke Jr, W.F., et al. *Asteroids III* ISBN 0-8165-2281-2, Pg 653-667

Carlson, R. W., Garnero, E., Harrison, T. M., Li, J., Manga, M., McDonough, W.F., Mukhopadhyay, S., Romanowicz, B., Rubie, D., Williams, Q., and Zhong, S. (2014) How Did Early Earth Become Our Modern World? *Annual Review Earth Planet. Sci*. 2014. 42:151–78 doi: 10.1146/annurev-earth-060313-055016

Carter, N.L., Raleigh, C.B., and Decarli, P.S. (1968) Deformation of Olivines in Stony Meteorites. *Journal of Geophysical Research*. Volume 73, Issue 16, Pg 5439-5461

Carter, N.L. and Ave'lallemant, H. G. (1970) High Temperature Flow of Dunite and Peridotite. *Geological Society of America Bulletin,* v. 81, p.2181-2202, 24 figs.

Chatzaras, V., Kruckenberg, S. C., Cohen, S. M., Medaris, G. Jr., Withers, A. C., and Bagley, B. (2016) Axial-type olivine crystallographic preferred orientations: The effect of strain geometry on mantle texture. *Journal of Geohphysical Research:Solid Earth.* https://doi.org/10.1002/2015JB012628

Downes H., Mittlefehlt, D. W., Kita, N. T., and Valley, J. W. (2008) Evidence from polymict ureilite meteorites for a disrupted and re-accreted single ureilite parent asteroid gardened by several distinct impactors. *Geochemica et Cosmochimica Acta* Volume 72, Issue 19, 4825-4844

Goodrich, C.A., Scott, E.R.D., and Fioretti, A.M. (2004) Ureilitic Breccias: Clues to the Petrologic Structure and Impact Disruption of the Ureilite Parent Body. *Chemie der Erde* 64 283-327

Hugo, H. C., Ruzicka, A. M., and Rubin A. E., (2018) Mesoscale and microscale shock effects in the LL6 S4 chondrites Saint-Severin and Elbert: A tale of two breccias. The Meteoritical Society. *Meteoritics & Planetary Science* 1–21 (2019) doi: 10.1111/maps.13304

Herrin J. S., Zolenky, M. E., Ito, M., Le, L., Mittlefehldt D. W., Jennkinson P., Ross A. J., and Shaddad M. H. (2010). Thermal and fragmentation history of ureilitic asteroids: Insights from the Almahata Sitta fall. *Meteoritics & Planetary Science* 45, Nr 10–11, 1789–1803 (2010) doi: 10.1111/j.1945-5100.2010.01136.x

Jamsja, N., and Ruzicka, A. (2010) Shock and thermal history of Northwest Africa 4859, an annealed impact-melt breccia of LL chondrite parentage containing unusual igneous features and pentlandite. *Meteoritics & Planetary Science* 1–22 (2010) doi: 10.1111/j.1945-5100.2010.01056.x

Karato S. Jung H., Katayama I., and Skemer P. (2008) Geodynamic significance of seismic anisotropy of the Upper Mantle: New Insights from Laboratory Studies. *Annual Review Earth Planet, Sci*. 36:59–95

Langdem A. D. Tomins A. G., Evans, K. A., Wilson N. C., MAcRAE C. M., Stephens N.R., and Torpy A. (2021) CHOS gas/fluid-induced reduction in ureilites. *Meteoritics & Planetary Science* 56, Nr 11, 2062–2082 (2021) doi: 10.1111/maps.13755

Leya I., and Stephenson P. C., (2019) Cosmic ray exposure ages for ureilites—New data and a literature study. *Meteoritics & Planetary Science* 54, Nr 7, 1512–1532 (2019) doi: 10.1111/maps.13288

McSween, H. Y. (1989) Achondrites and Igneous Processes on Asteroids: *Annual Review Earth Planet, Sci.* 17:119-40

Meteoritical Bulletin Database (2022) *The Meteoritical Society* https://www.lpi.usra.edu/meteor/ Last updated Apr 23, 2022

Michel, P., Jutzi, M., Richardson, D. C., Goodrich, C. A., Hartmann, W. K., and O'Brien, D.P. (2014) Selective sampling during catastrophic disruption: Mapping the location of reaccumulated fragments in the original parent body. *Planetary and Space Science* 107 24-28

Nestola, F., Goodrich, C. A., Morana, M., Barbaro, A., Jakubek, R. S., Christ, O., Brenker, F. E., Domeneghetti, M. C., Dalconi, M. C., Alvaro, M., Fioretti, A. M., Litasov, K. D., Fried, M.D., Leoni, M., Casati, N. P. M., Jenniskens, P., and Shaddad M. H. (2020) Impact shock origins of diamonds in ureilite meteorites. *The*

Proceedings of the National Academy of Sciences
https://doi.org/10.1073/pnas.1919067117

Prior, D. J., Mariani, E., and Wheeler, J. (2009) EBSD in the Earth Sciences: Applications, Common Practice, and Challenges. In, A.J. Swartz et al. (eds.), *Electron Backscatter Diffraction in Materials Science,* DOI 10.1007/978-0-387-88136-2_26,

Rai N., Downes, H., and Smith, C. (2020) Ureilite meteorites provide a new model of early planetesimal formation and destruction. *Geochemical Perspective Letters* 14, 20-25.

Ruzicka A., and Hugo R. (2022) Model Deformation Temperatures derived from EBSD for olivine in type 6 ordinary chondrites and ureilites. *LPSC abstract* #1757

Stöffler, D., Keil, J.K., and Scott, E. R. D. (1991) Shock metamorphism of ordinary chondrites 'Planetary Geosciences Division, Department of Geology and Geophysics, School of Ocean and Earth Science and Technology, University of Hawaii at Manoa, Honolulu, HI 96822, US

National Aeronautics and Space Administration (NASA) (2021) Lucy: The First Mission to the Trojan Asteroids https://www.nasa.gov/mission_pages/lucy/overview/index Last updated Sep 27 2021

Wallis D., Hansen L. N., Tasaka, M., Kumamoto, K. M., Parsons, A. J., Lloyd, G. E., Kohlsted, D. L., and Wilkinsons, A.J., (2018) The impact of water on the slip system activity in olivine and the formation of the bimodal crystallographic preffed orientations. *Earth and Planetary Science Letters* Volume 508, 15 February 2019, Pages 51-61

Welsch, B., Faure, F., Famin, V., Baronnet, A., and Bachelery, P. (2013) Dendritic Crystallization: A Single Process for all the Textures of Olivine in Basalts? *Journal of petrology* Volume 54 N3 Pg:539-574 doi:10.1093/petrology/egs077

Wilson, L., Orman J.A., and Goodrich, C. A. (2008) Thermal evolution and physics of melt extraction on the ureilite parent body. *Geochimica et Cosmochimica Acta* Volume 72, Issue 24, 15 December 2008, Pages 6154-6176

Appendix A: Petrographic Thin Sections

NWA 11993 PPL

NWA 11993 XPL

NWA 12433 PPL

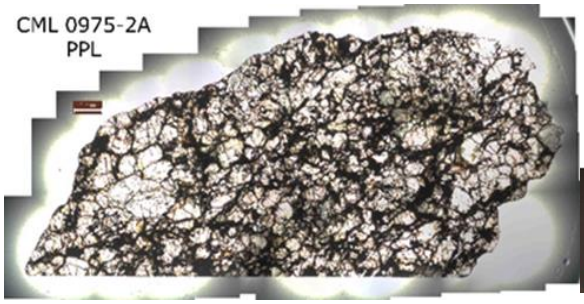

NWA 12433 XPL

NWA 7630 PPL

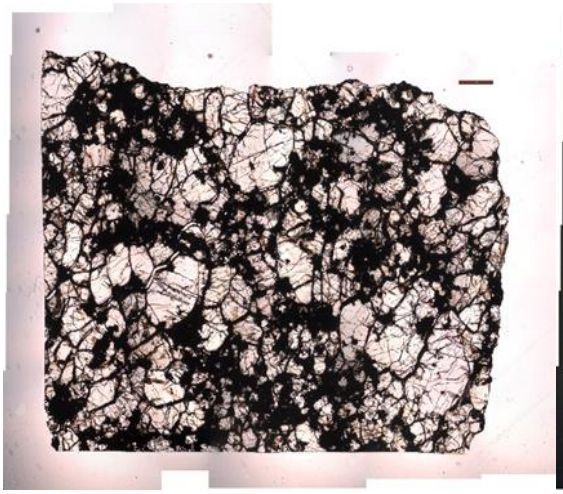

NWA 7630 XPL

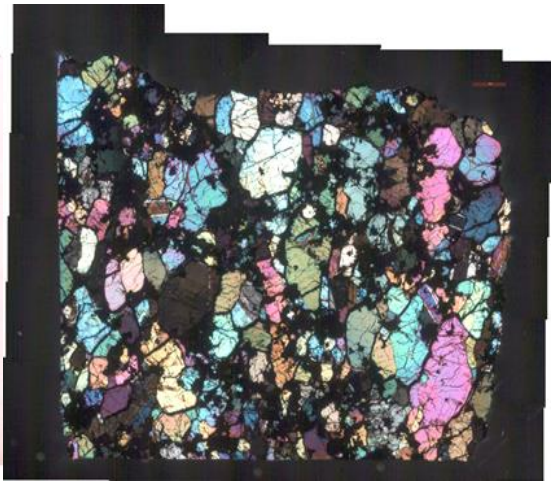

NWA 7304 PPL

NWA 7304 XPL

Appendix B: EBSD Maps

NWA 11993

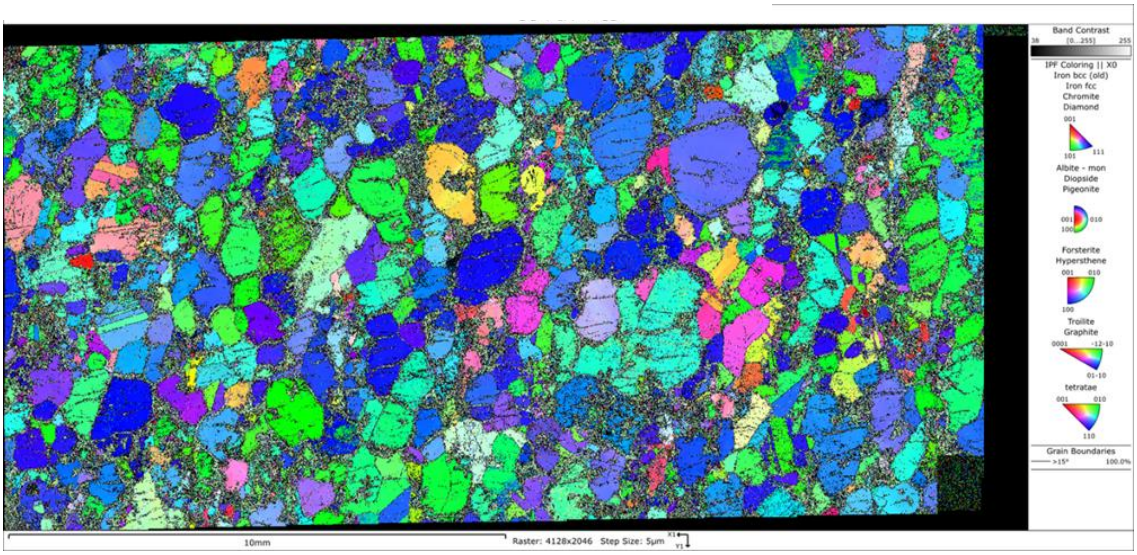

NWA 12433

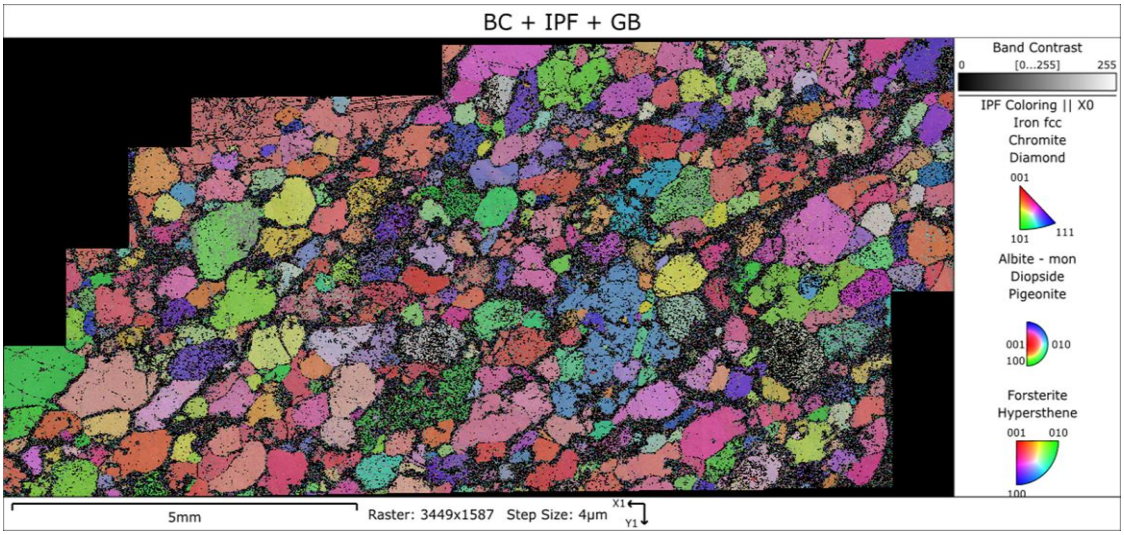

NWA 7630

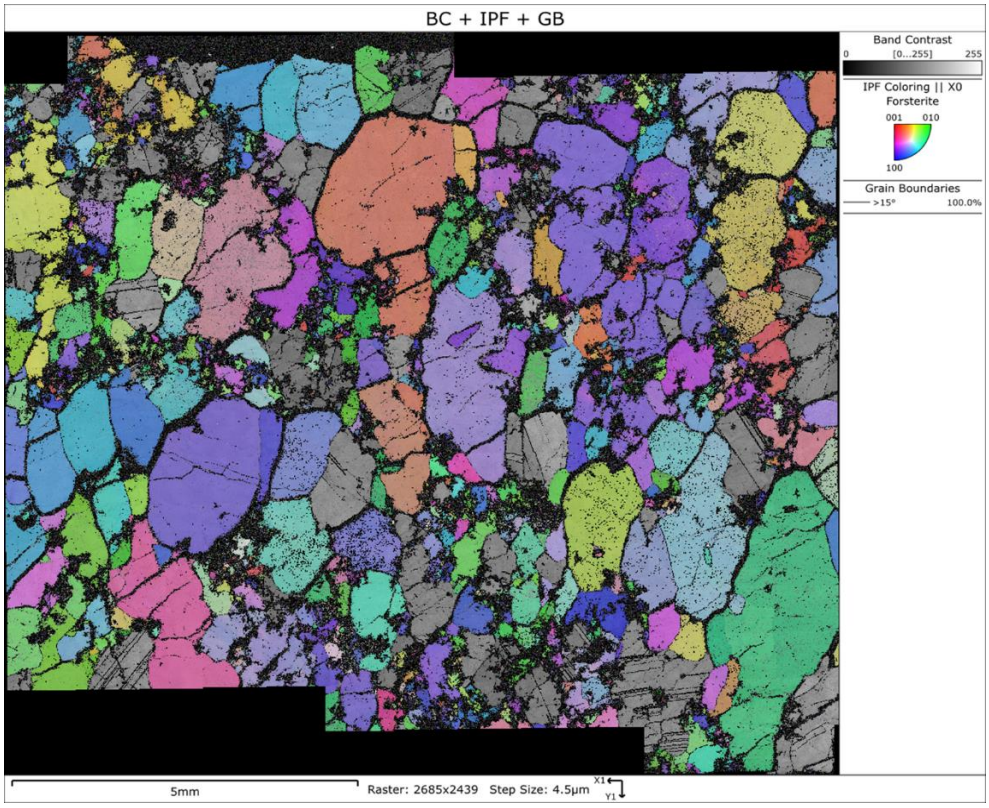

NWA 7304

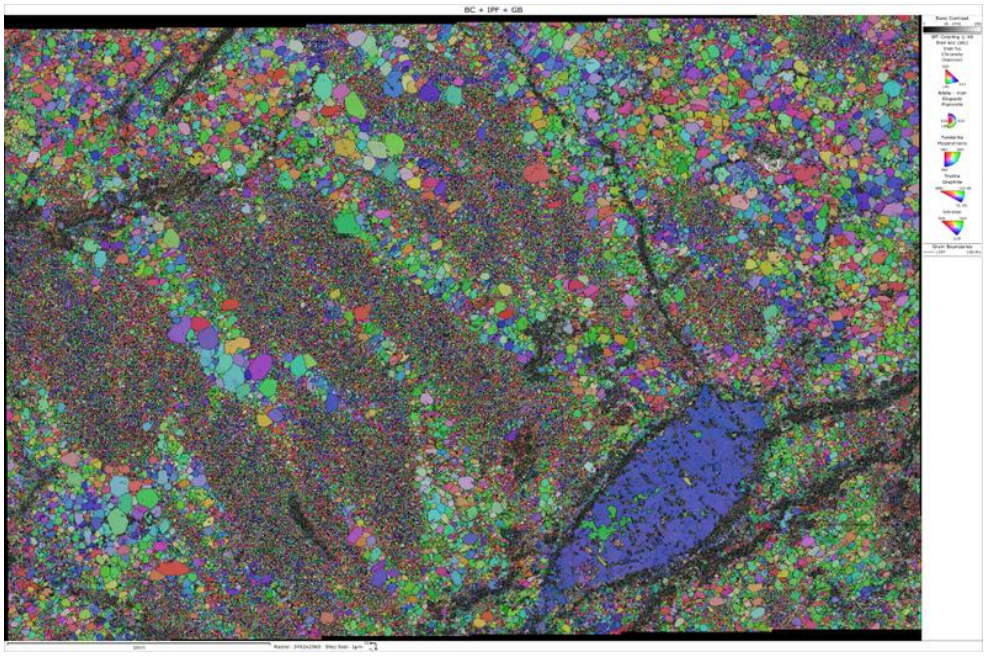

NWA 11993

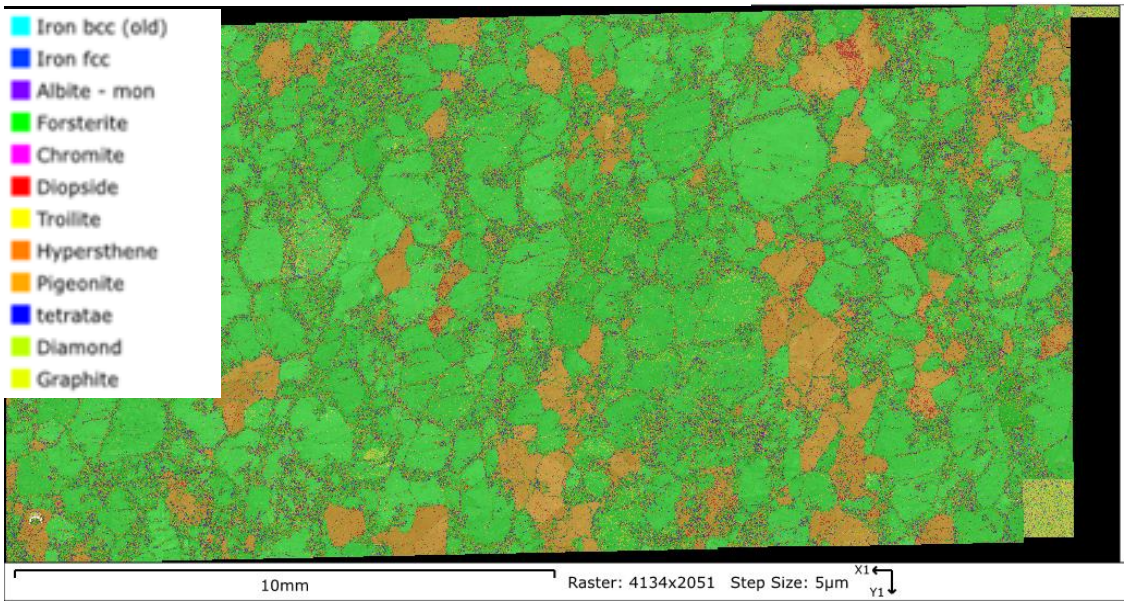

NWA 12433

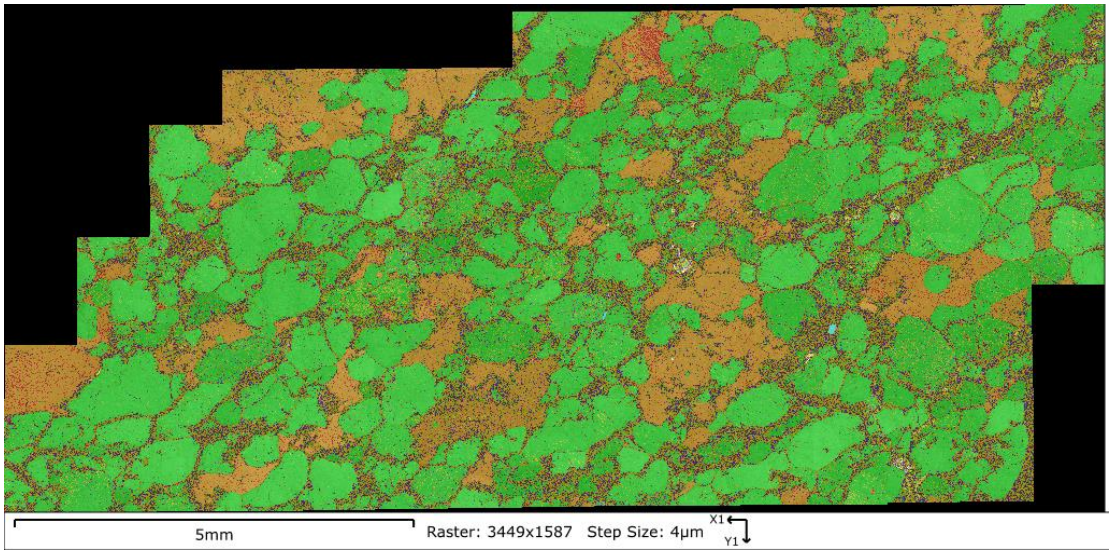

NWA 7630

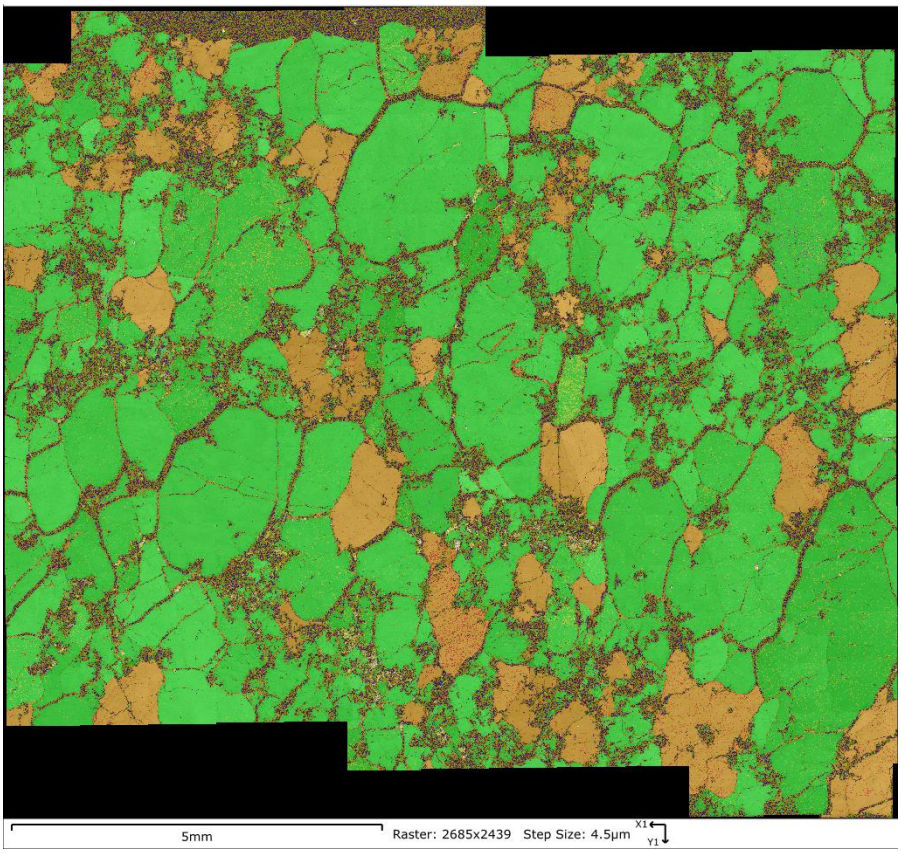

NWA 7304

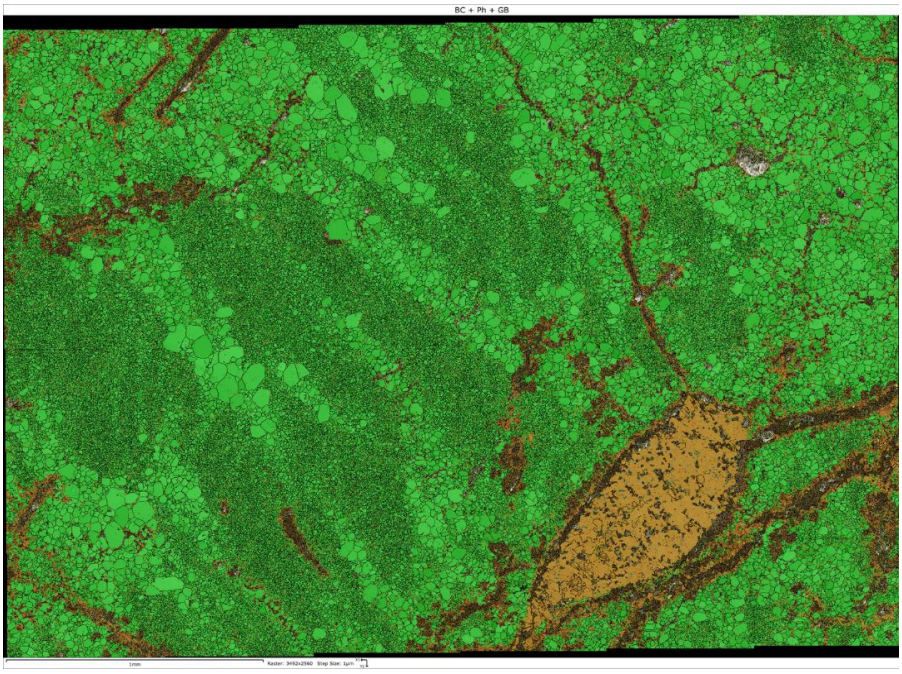

NWA 11993

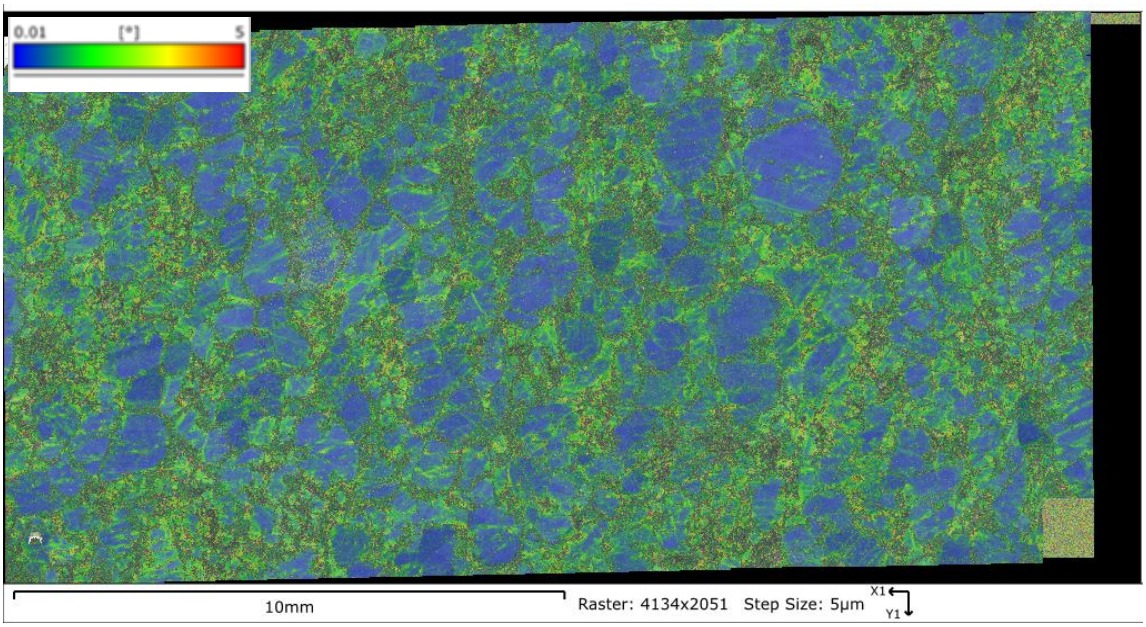

NWA 12433

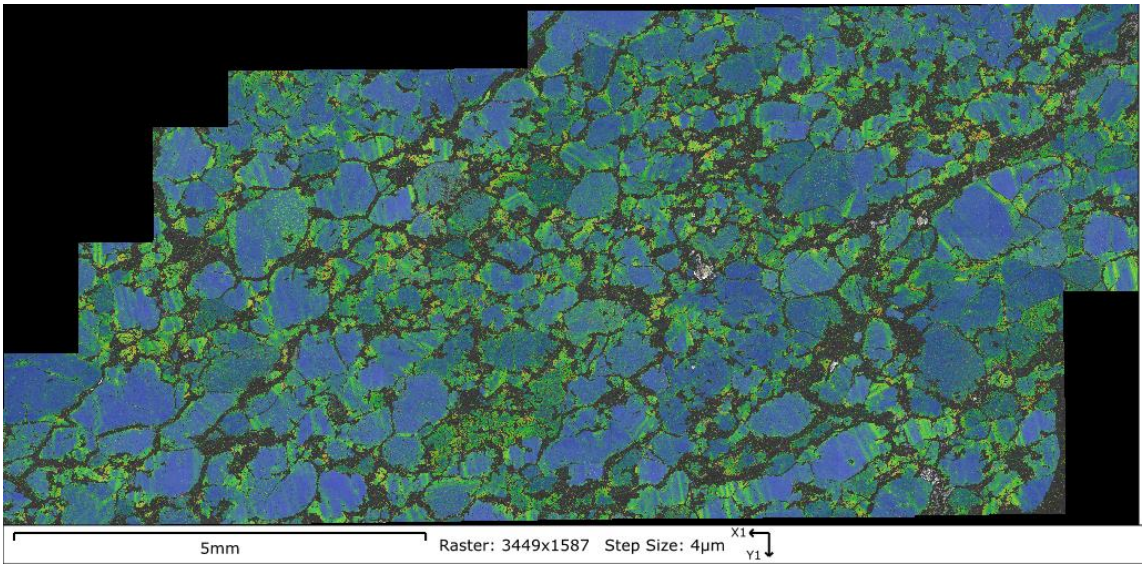

NWA 7630

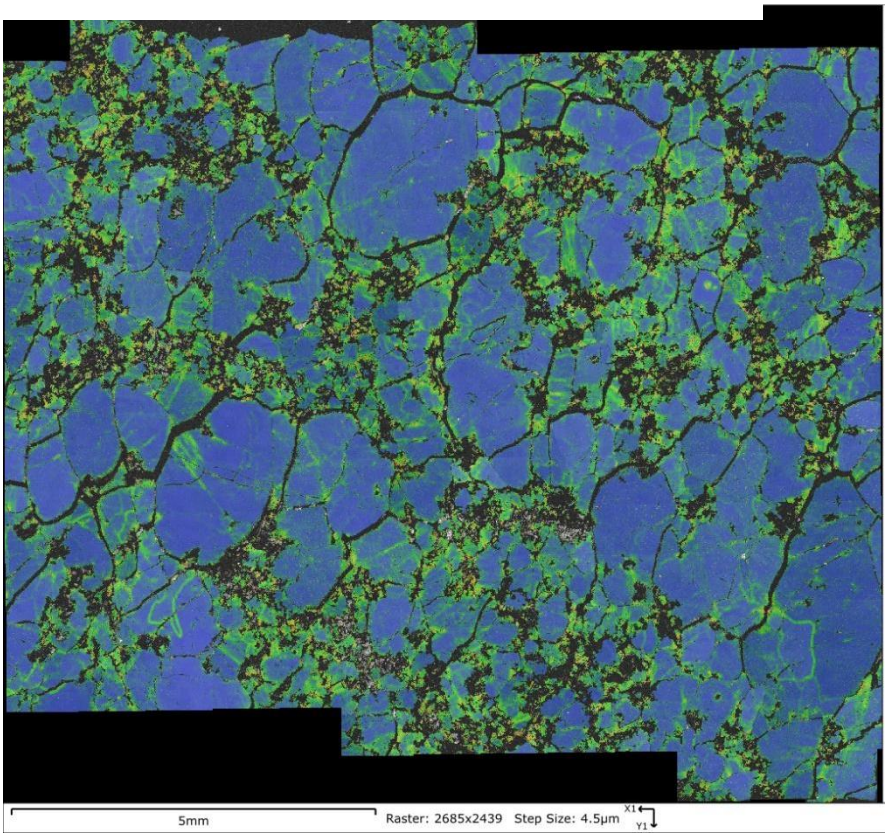

NWA 7304

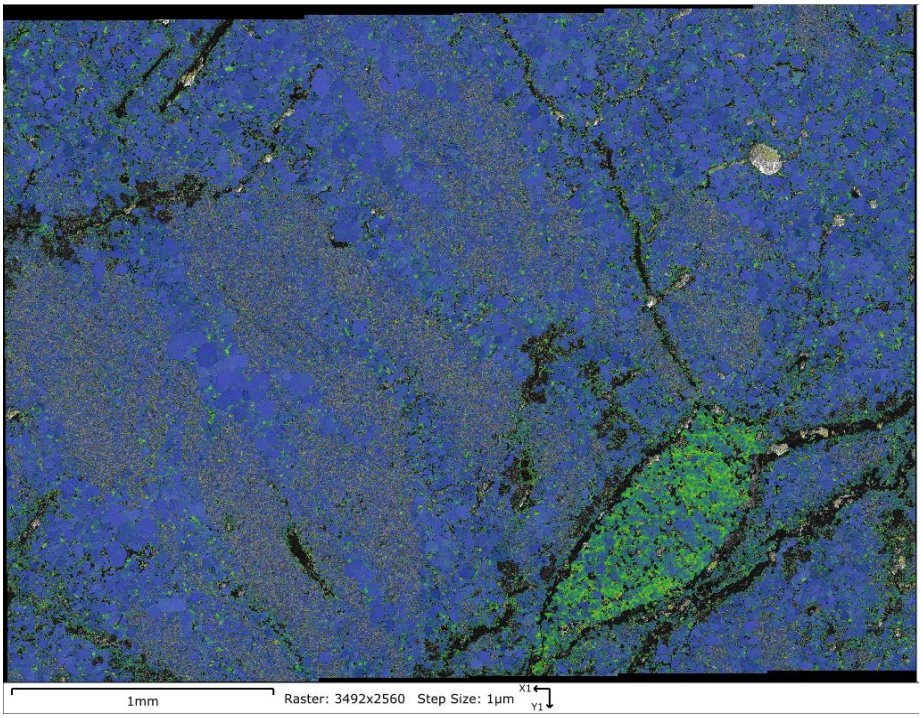

NWA 11993

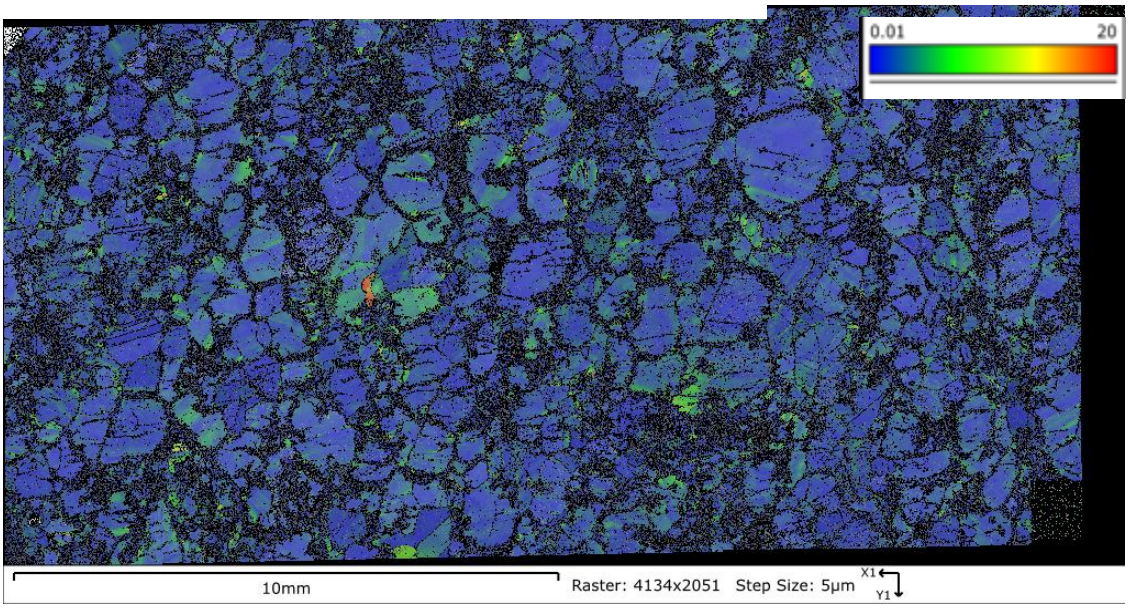

NWA 12433

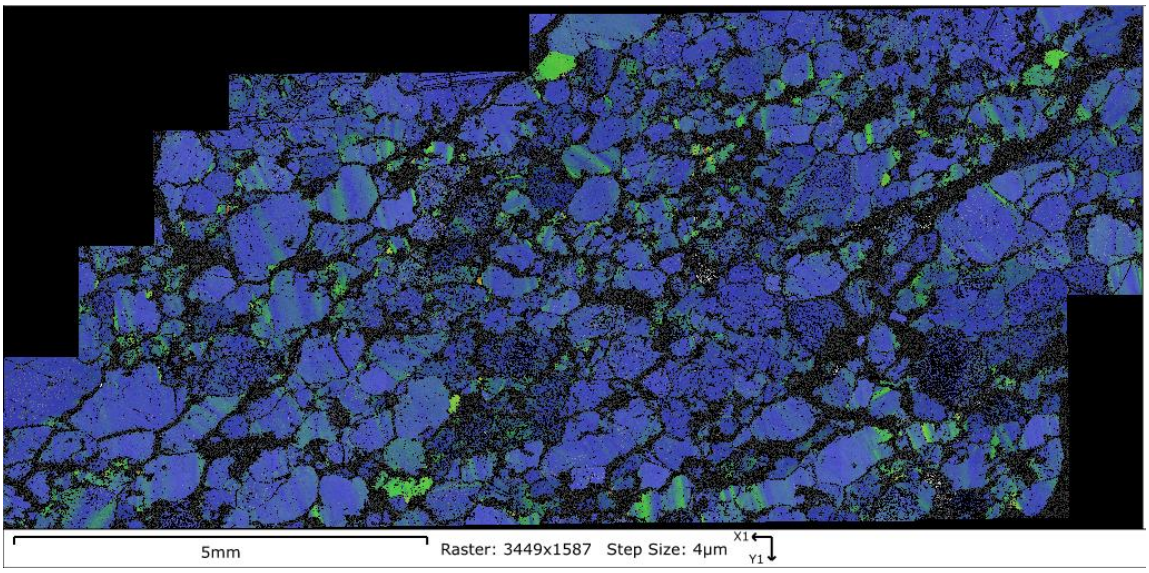

NWA 7630

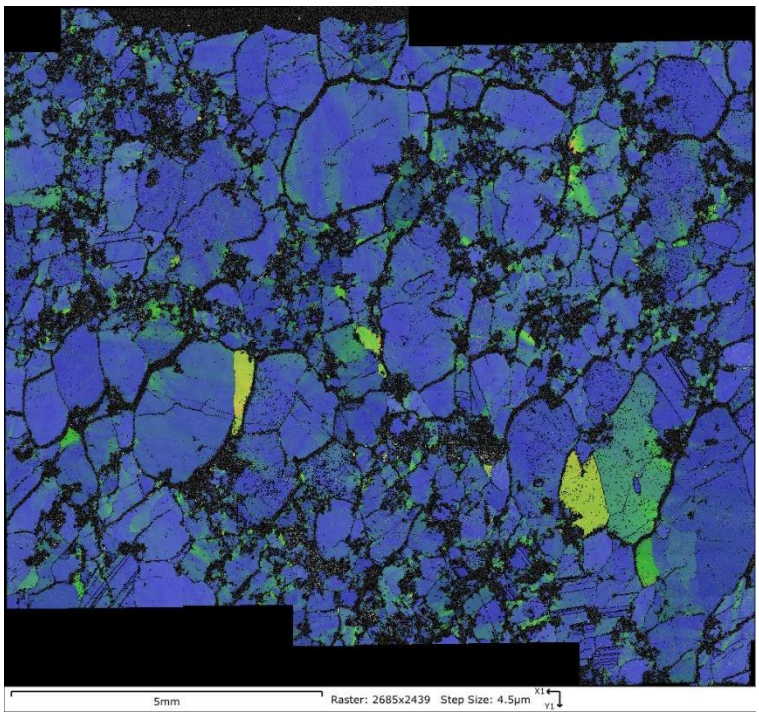

NWA 7304

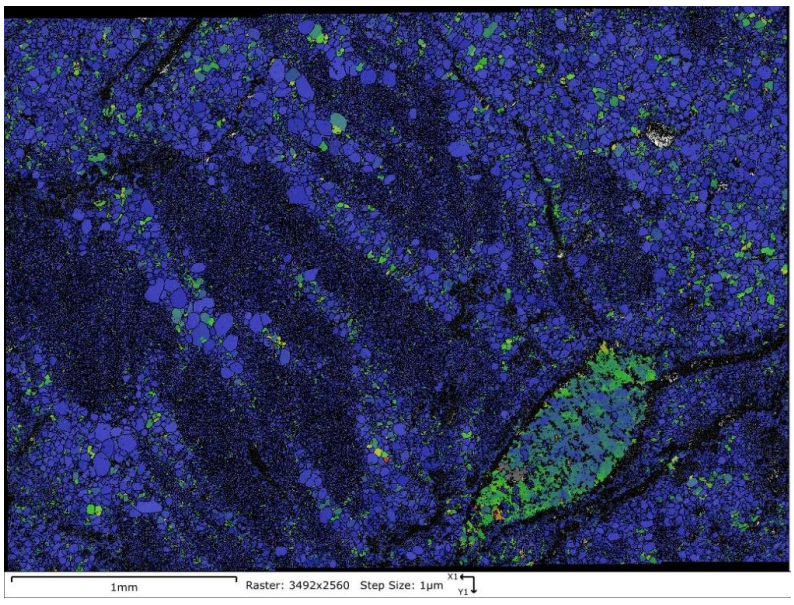

NWA 11993

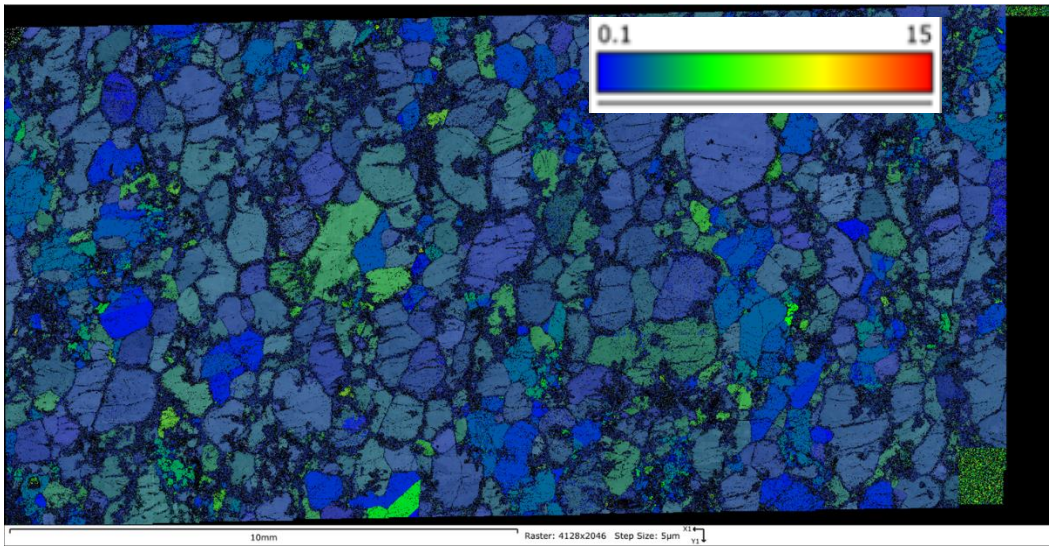

NWA 12433

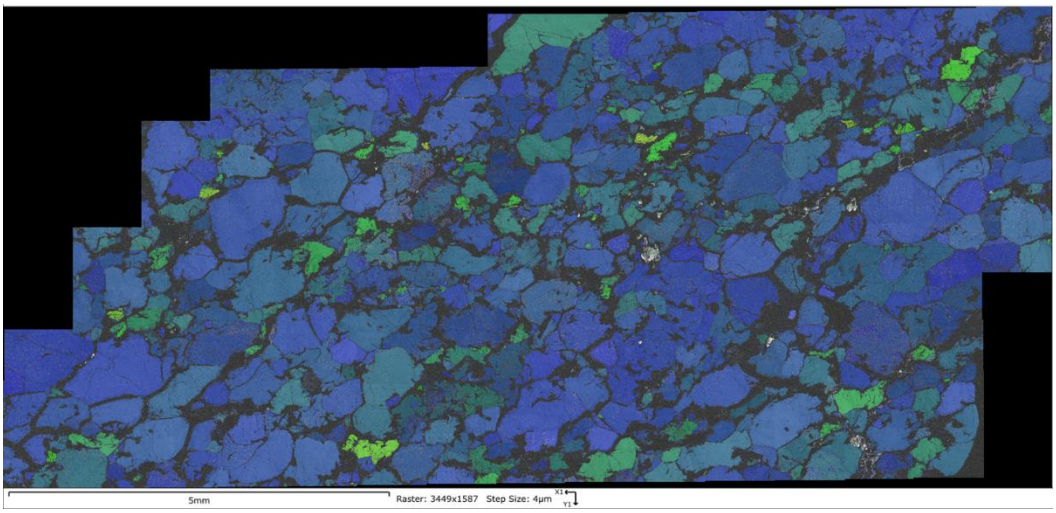

NWA 7630

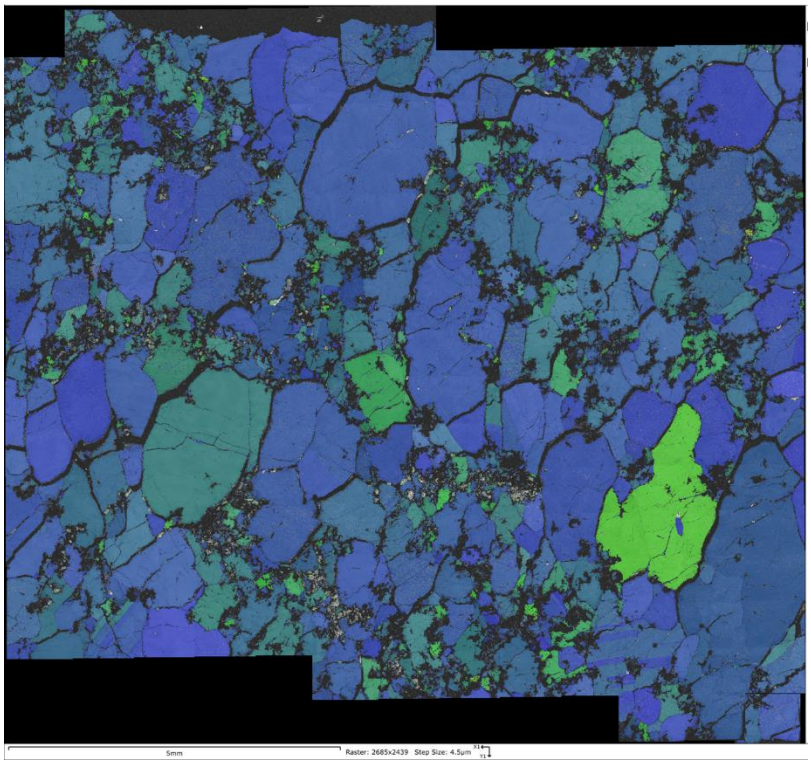

NWA 7304

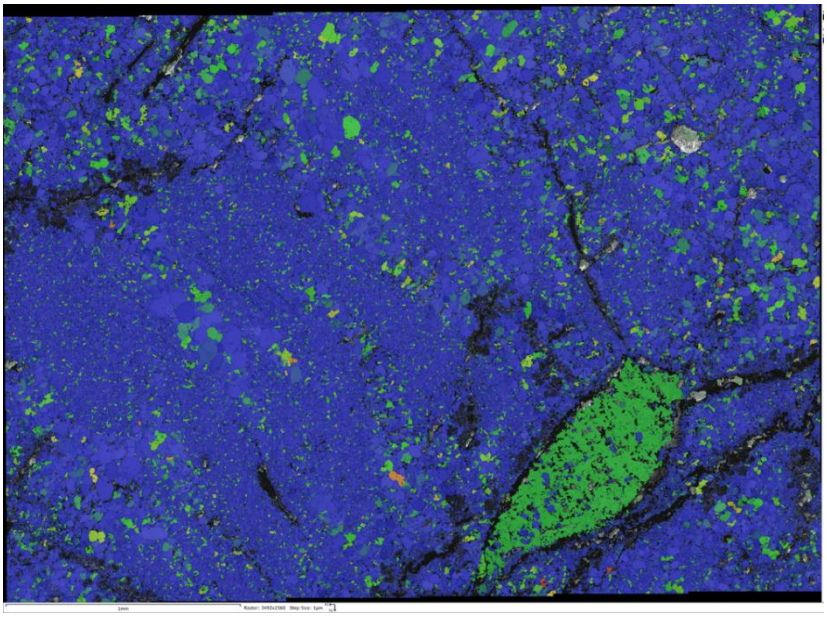

NWA 11993 Coarse

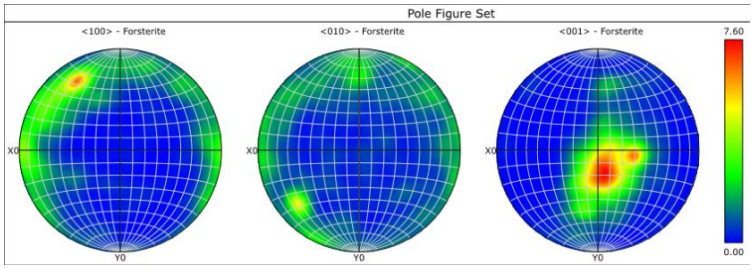

NWA 11993 Fine

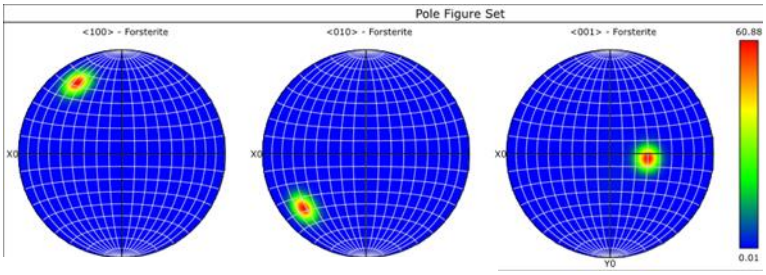

NWA 12433 Coarse

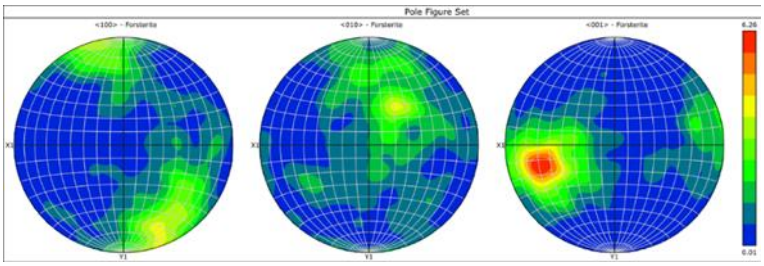

NWA 12433 Fine

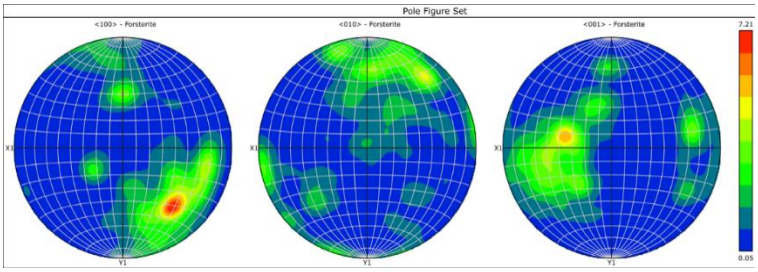

NWA 7630 Coarse

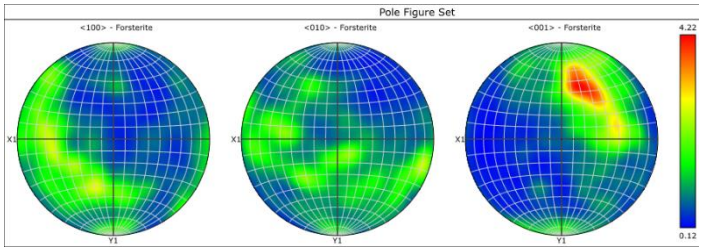

NWA 7630 Fine

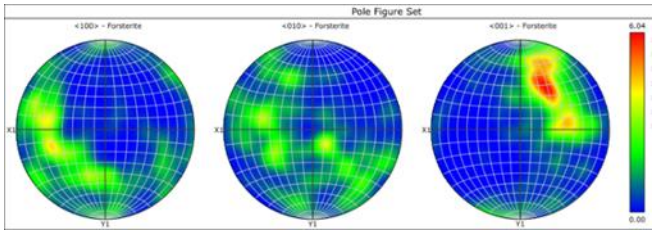

NWA 7304 Coarse

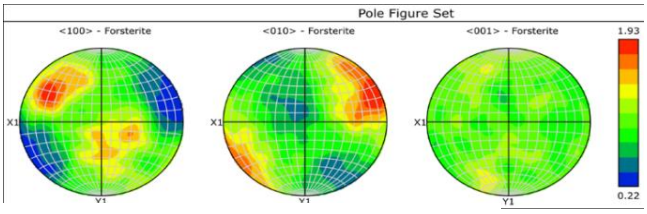

NWA 7304 Fine